Impact of Mixed-Phase Cloud Parameterization on Warm Conveyor Belts and Upper-Tropospheric Dynamics

Marie Mazoyer, Didier Ricard, Gwendal Rivière, Julien Delanoë, Sébastien Riette, Clotilde Augros, Mary Borderies, Benoit Vie

To cite this version:

Marie Mazoyer, Didier Ricard, Gwendal Rivière, Julien Delanoë, Sébastien Riette, et al.. Impact of Mixed-Phase Cloud Parameterization on Warm Conveyor Belts and Upper-Tropospheric Dynamics. Monthly Weather Review, 2023, 151 (5), pp.1073-1091. 10.1175/MWR-D-22-0045.1 . hal-04275909

HAL Id: hal-04275909

https://hal.science/hal-04275909v1

Submitted on 8 Nov 2023

Impact of mixed-phase cloud parameterization on warm conveyor belts and upper-tropospheric dynamics

Marie Mazoyer,[a] Didier Ricard,[a] Gwendal Rivière,[b] Julien Delanoë,[c] Sébastien Riette,[a]
Clotilde Augros,[a] Mary Borderies,[a] Benoit Vié[a]

[a] *CNRM, Université de Toulouse, Météo-France, CNRS, Toulouse, France*
[b] *LMD/IPSL, École Normale Supérieure, PSL Research University, École Polytechnique, Sorbonne Universités, CNRS, Paris, France*
[c] *LATMOS-IPSL, CNRS/INSU, University of Versailles, Guyancourt, France*

Corresponding author: Marie Mazoyer, marie.mazoyer@yahoo.fr

ABSTRACT: This study investigates mixed-phase cloud (MPC) processes along the warm conveyor belts (WCBs) of two extratropical cyclones observed during the North Atlantic Waveguide and Downstream Impact EXperiment (NAWDEX). The aim is to investigate the effect of two radically distinct parameterizations for MPCs on the WCB and the ridge building downstream; the first one (REF) drastically limits the formation of liquid clouds while the second one (T40) forces the liquid clouds to exist. REF exhibits a stronger heating below 6 km height and a more important cooling above 6 km height than T40. The stronger heating at lower levels is due to more important water vapor depositional processes while the larger cooling at upper levels is due to differences in radiative cooling. The consequence is a more efficient potential vorticity destruction in the WCB outflow region and a more rapid ridge building in REF than T40. A comparison with airborne remote sensing measurements is performed. REF does not form any MPCs whereas T40 does, in particular in regions detected by the radar-lidar platform like below the dry intrusion. Comparison of both ice water content and reflectivity shows there may have too much pristine ice and not enough snow in REF and not enough cold hydrometeors in general in T40. The lower ice to snow ratio in T40 likely explains its better distribution of hydrometeors with respect to height compared to REF. These results underline the influence of MPC processes on the upper-tropospheric circulation and the need for more MPC observations in mid-latitudes.

SIGNIFICANCE STATEMENT: The diabatic processes occurring in the warm conveyor belt (WCB) of extratropical cyclones impact the jet stream structure at mid-latitudes. This study highlights some sensitivity of upper-level dynamics to mixed-phase cloud related processes. Comparisons of two different microphysical schemes for mixed-phase clouds shows that the ratio of liquid to solid clouds along the WCB ascents impacts the latent heat release and the radiation. Data from the NAWDEX campaign helps to determine rooms for improvements for both schemes and point out the need of a better understanding of these processes for an improved prediction of upper-level dynamics.

1. Introduction

Mid-latitude atmospheric circulation has been shown to be strongly dependent on diabatic processes occurring in the warm conveyor belts (WCBs) of extratropical cyclones (Pomroy and Thorpe 2000; Grams et al. 2011, among many others). WCBs are ascending coherent warm and moist airstreams rising from the boundary layer to the upper troposphere and forming elongated cloud bands (Harrold 1973; Browning 1986). When these airstreams ascend, liquid, mixed-phase, and ice clouds form and the corresponding latent heat release can warm the air as much as 20 K in 48 h (Madonna et al. 2014; Joos and Forbes 2016). Cloud thermodynamic phase impacts on dynamics can be described through the potential vorticiy (PV) framework (Hoskins et al. 1985). PV increases below the maximum of heating in the lower troposphere and decreases above it at the level of the jet stream. Misrepresented diabatic processes may lead to the formation of PV forecast errors that propagate and grow along the jet stream (Dirren et al. 2003; Gray et al. 2014; Martínez-Alvarado et al. 2016) and produce consequences on the downstream predictability of high-impact weather events. This reasoning mainly motivated the international field campaign NAWDEX (North Atlantic Waveguide Downstream and impact EXperiment) that occurred in September-October 2016 (Schäfler et al. 2018).

An on-going challenge in Numerical Weather Prediction (NWP) and climate modelling concerns the representation of mixed-phase clouds (MPCs) (Illingworth et al. 2007) that are composed of supercooled cloud droplets (i.e. under 0 °C) and ice crystals. Liquid fraction within MPCs is invariably underestimated in models according to Tremblay et al. (2003) and Morrison et al. (2003). MPCs are thermodynamically unstable because saturation with respect to ice is reached at lower humidity than with respect to liquid. However, according to Shupe et al. (2008) and McFarquhar et al. (2011), supercooled cloud droplets can persist from several hours to several days before the transition to solid phase occurs. MPCs have been extensively studied for their climatic significance trough radiation (Sun and Shine 1994), for their impact on precipitation enhancement (Korolev et al. 2017) and because they are responsible of hazardous aircraft icing (Cober et al. 2001). Some studies focused on their dynamical impact on convection enhancement (Seifert and Beheng 2006; Kumar et al. 2014), but to our knowledge no studies explored their impact on mid-latitude upper-tropospheric dynamics. MPCs experience the three different water phase changes during their formation and evolution: vapor to liquid, vapor to solid and liquid to solid. Latent heat releases associated with these three different phase transitions differ strongly so that the mixing partition may impact the heating rates by ~ 10 % (Yau and Rogers 1996).

High occurrence of supercooled water in the North Atlantic has been reported by Hu et al. (2010) and Mülmenstädt et al. (2015) and evidence of MPCs within WCBs of extratropical cyclones have been observed by Boettcher et al. (2021) and Alexander et al. (2021). MPCs are more likely to occur when vertical velocities are strong enough so that liquid water vaporsaturation can be reached (Korolev et al. 2017). In WCBs, embedded convection (Rasp et al. 2016; Oertel et al. 2019; Gehring et al. 2020) may allow these conditions to occur. Also, radiation and turbulent mixing with clear air at the top or at the edge of the cloud may favor the occurrence of liquid water supersaturation at temperatures well below 0 °C according to Korolev and Mazin (2003).

The present study follows two main objectives: the first one is to document the occurrence of MPCs within the WCBs using the dataset of the NAWDEX campaign and the second one is to investigate how the representation of MPCs in numerical models can impact the jet stream in the WCB outflow region. To achieve the first objective, unique observations of cloud water thermodynamic phases are analysed using the measurements made with both the Doppler radar RASTA (RAdar SysTem Airborne) and the lidar LNG (Leandre New Generation) (Delanoë et al. 2013b) on board the French SAFIRE (Service des Avions Français Instrumentés pour la Recherche en Environnement) Falcon 20. To reach the second objective, numerical simulations of the Meso-NH model (Lac et al. 2018) with two different representations for MPCs have been performed and are hereafter analyzed.

Two extratropical cyclones intensively observed during NAWDEX have been analysed and simulated. The first extratropical cyclone is associated with a strong synoptic forcing. It is called the 'stalactite' cyclone and corresponds to the Intensive Observation Period (IOP) 6. The second one is associated with a moderate synoptic forcing that led to the formation of the tropopause ridge 'Thor' and corresponds to IOP 10. The terms stalactite cyclone and Thor ridge come from specific shapes in the PV field during the formation of these phenomena (Schäfler et al. 2018). It is worth investigating these two events because they are triggered with distinct synoptic forcings and also because the dynamical response to diabatic heating is known to be highly case-dependent (Smith 2000). The sensitivity to the pre-existing hydrometeor distribution will also be considered as the results could strongly vary from one initial state to another (Berman and Torn 2019).

In a companion paper (Mazoyer et al. 2021, hereafter denoted as MAZ21), simulations of the stalactite cyclone have been already performed using the one-moment microphysical scheme ICE3 (Pinty and Jabouille 1998) and compared to a quasi-two-moment microphysical scheme, called LIMA (Vié et al. 2016). Differences between the two schemes on the WCB of the stalactite cyclone and the jet stream aloft were found to be important after 2-day simulations. The study of MAZ21, showed that the ICE-3 microphysics has better skills than the complex two-moment scheme LIMA (Vié et al. 2016) to simulate the WCB and the ridge building downstream.

In the present study, the same approach as in MAZ21 is followed but instead we are comparing two different representations of MPCs within ICE3 and analyzing two case studies instead of only one. ICE3 uses a simple saturation adjustment scheme (Lord et al. 1984) based on the assumption that the entire supersaturated water vapor condenses. The saturation mixing ratio is defined as the mass-weighted average of the respective saturation values over liquid and ice. A first possibility in ICE3 is then to adjust water vapor on droplets and pristine ice in proportion to their amount before the adjustment. A second possibility (Tao et al. 1989) is to force the vapor adjustment in a way, that at the end of all the microphysical steps, the sum of water mass due to droplets and pristine ice is distributed between droplets and pristine ice according to a linear function of temperature from 0 to -40 °C. Such a parameterization allows both hydrometeors to coexist at temperatures as low as -40 °C (DeMott and Rogers 1990; Rosenfeld and Woodley 2000; Hu et al. 2010). While the first method is highly dependent on initial conditions (Engdahl et al. 2020), the second one forces the hydrometeor distribution (Boudala et al. 2004). Obviously both methodshave advantages and drawbacks, but should proceed to different liquid and solid partitions which rightly allows us to investigate the impact of this partition on large-scale dynamics.

The structure of the paper is as follows: section 2 is dedicated to the methodology and the synoptic overview of the two cases. Section 3 describes the microphysical characteristics of the simulations made with the two distinct parameterizations, their differences in latent heat release and their distinct impacts on the upper-level ridge building. Section 4 compares model simulations and airborne radar-lidar observations in terms of thermodynamic phases and microphysics products in an attempt to document the occurrence of MPCs and to assess the skills of the two microphysical schemes. Discussions and conclusions are drawn in section 5.

2. Methodology and case description

a. Model

The French anelastic research model Meso-NH (Mesoscale Non-Hydrostatic) (Lac et al. 2018, http://mesonh.aero.obs-mip.fr/) is used in a convection-permitting mode at a 2.5 km horizontal grid spacing with 55 stretched vertical levels. All the parameterizations are the same as in MAZ21. Only the setup of the microphysical scheme ICE3 (Caniaux et al. 1994; Pinty and Jabouille 1998) may differ from MAZ21 in some experiments. ICE3 is a bulk mixed-phase one-moment microphysical scheme with prognostic equations predicting the mass mixing ratios of six water species (water vapor, droplets, rain, pristine ice, snow, and graupel). In cold clouds, snow is only formed by autoconversion and aggregation of pristine ice. As graupel is a MPC hydrometeor, it is first formed by rain or droplets collection by ice or snow and can then grow by vapor deposition. An adjustment to saturation for liquid/solid phase is performed meaning that there is deposition of all the excess vapor on cloud droplets/pristine ice particles in warm/cold clouds. In our reference version (called REF), a barycentric formula based on pristine ice and cloud droplets mass mixing ratio before the adjustment is used to divide the excess vapor between pristine ice particles and cloud droplets, which may lead to artificial distribution between hydrometeors. However, an option, that we call T40, is to distribute the vapor in order to respect a ratio between droplets and pristine ice as a linear function of temperature from 0 to -40 °C at the end of the microphysics (all other source/sink terms computed). Consequently with that option, above 0 °C only liquid is present and under -40

°C only pristine ice. While this second option appears even less physical, it gets the advantage of being radically opposite to the REF options as it forces the MPCs to exist.

b. Synoptic overview and simulation set up

Two extratropical cyclones and associated upper-level ridges that contributed to the onset and persistence of a blocking event over Scandinavia during the period 2–19 October 2016 are hereafter studied. These events are presented in Schäfler et al. (2018, see their Fig.6) and Steinfeld et al. (2020, see their Fig.1) and can be summarized as follows:

- The stalactite cyclone observed during IOP 6 of NAWDEX explosively deepened with a sea level pressure (SLP) decrease of 26 hPa in 24h. The associated upper-level ridge initiated the block onset (Maddison et al. 2019; Steinfeld et al. 2020) and has been already extensively studied using different models and observations (Blanchard et al. 2020, 2021; Flack et al. 2021; Mazoyer et al. 2021; Rivière et al. 2021).

- The extratropical cyclone associated with the Thor ridge and observed during IOP 10 of NAWDEX was less intense. The Thor ridge is one of the last ridges that contributed to the agglomeration and persistence of the Scandinavian block (Schäfler et al. 2018; Sánchez et al. 2020; Steinfeld et al. 2020).

The REF and T40 configurations of the model are run for both cases. Because initial conditions may impact the WCB representation (Berman and Torn 2019), sensitivity to the initial state is made for the stalactite cyclone. Overall, six simulations are run, with initial and lateral boundary conditions provided by 6-hourly global operational model ARPEGE analyses:
(i) The stalactite cyclone initialized at 00 UTC 1 October 2016 lasting 48 hours.
(ii) The stalactite cyclone initialized at 12 UTC 1 October 2016 lasting 36 hours.
(iii) The Thor ridge initialized at 12 UTC 11 October 2016 lasting 36 hours.
The three initial states of the two cyclone events are localized in the southwestern part of the Meso-NH domain at the initial times (Figs. 1a, b and d). The stalactite cyclone is deeper, the circulation is less zonal and the ridge building is more developed in the initial state of (ii) than (i) (see Figs. 1a,b). In (iii), the initial state is composed of a surface low which is only half visible at

40°W, 50°N in Fig. 1d, a well-developed Scandinavian block and a decaying cyclone near 37° W, 62° N. Flights with the French SAFIRE Falcon 20 were conducted during the deepening phase of both extratropical cyclones in order to sample the ascending branch of the WCB that is associated with intense cloud formation. A good area to examine is located ahead of the surface cold front in the warm sector of the cyclone that corresponds to the ascending part of the WCB. Figs. 1c and e show the surface cold front position in terms of potential temperature at 850 hPa during the time of the selected flights of the NAWDEX campaign. During the stalactite cyclone, the Falcon flight numbered F7 (Fig. 1c) sampled the WCB south of Iceland from 1301 to 1616 UTC on 2 October. During the Thor ridge, the Falcon flight numbered F15 (Fig. 1e) sampled the WCB south of Iceland from 1551 UTC to 1825 UTC on 12 October.

c. Observations

During NAWDEX, the Falcon was equipped with a radar-lidar platform (RALI; (http://rali.projet.latmos.ipsl.fr/, Delanoë et al. 2013b). The radar measurements provide reflectivity and three-dimensional wind components. The combination of the Doppler radar RASTA and the lidar, is unique to get detailed information on clouds (combining the high sensitivity of the lidar and the penetration capability of the radar in thicker clouds). Thanks to the variational algorithm of Delanoë and Hogan (2008) and its further development (Delanoë and Hogan 2010; Cazenave et al. 2019), the radar-lidar measurements allow the retrieval of Ice Water Content (IWC) and provide a cloud classification. The major source of uncertainty comes from the choice of the mass law. More information on the uncertainties of retrievals can be find in Delanoë et al. (2013a) and Cazenave et al. (2019). The cloud thermodynamic phases are categorized in liquid, mixed phase, pristine ice, clear-sky and an 'unknown' category. Note that in our classification, under 0 °C, supercooled liquid water is encompassed in the mixed-phase cloud category. The radar RASTA is very sensitive to large hydrometeors (snow, graupel, rain) and the lidar to smaller ones (pristine ice or liquid cloud droplets). Moreover, the lidar signal is highly attenuated in optically thick clouds and by supercooled layers. The radar signal is less attenuated in the ice levels and is able to provide reflectivity observations at a high vertical resolution in deep cloud systems, as well as around the melting layer.

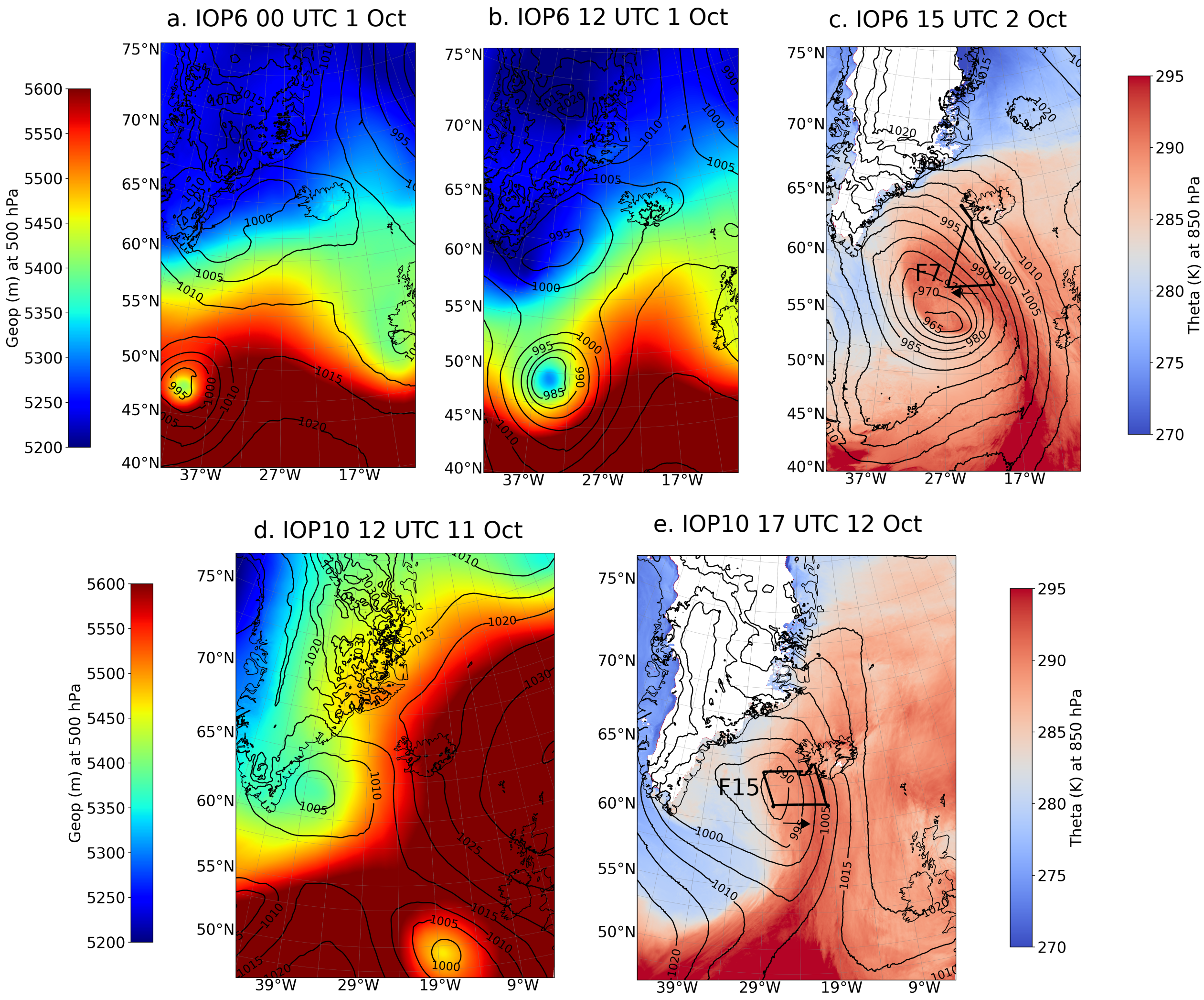

Figure 1. Geopotential height at 500 hPa and SLP (black contours; int: 5 hPa) from ARPEGE operational analysis at: (a) 00 UTC 1 Oct, (b) 12 UTC 1 Oct, (c) 12 UTC 11 Oct. Potential temperature at 850 hPa from the reference simulation and SLP at: (d) 15 UTC 1 Oct, (e) 17 UTC 12 Oct. The flight tracks are shown by the bold lines in c and e. F7 (IOP6) has a clockwise path and F15 (IOP10) an counter-clockwise path.

d. Model tools

1) RADAR SIMULATOR

To evaluate the simulations with respect to the RALI measurements, as in MAZ21, two moments of the hydrometeor particle size distribution (PSD) are compared: the third order corresponding to the IWC and the sixth order corresponding to the reflectivity. This double assessment requires a retrieval of the IWC from the RALI outputs and to derive the reflectivity from the model outputs. Both derivations have their own assumptions of hydrometeor shape, density, etc. and underlying algorithms. While hydrometeors were assumed to be spherical (using the Mie scattering theory) in MAZ21 to simulate the reflectivity from the model outputs, they are simulated as oblate spheroids in the present study using the T-matrix scattering theory (Mishchenko et al. 1996). The radar forward operator developed by Augros et al. (2016) and adapted to RASTA by Borderies et al. (2018) is used, with the axis ratios recommended by Borderies et al. (2018) for graupel (0.8), snow (0.7) and pristine ice (1). The forward operator accounts for hydrometeor and water vapor attenuation. No mixed-phase hydrometeors are explicitly represented in ICE3. A simple melting or wet growth model is thus used within the radar simulator: graupel particles are considered wet when they coexist with rainwater, and their liquid water fraction is estimated as $F_w = \frac{M_r}{M_r + M_g}$ with M_r and M_g the hydrometeor contents of rain and graupel.

2) Trajectories

To identify WCB air masses, backward Lagrangian trajectories are computed using the online algorithm of Gheusi and Stein (2002) as in MAZ21. Information on trajectories is given every 15 minutes on a 2.5 km × 2.5 km horizontal grid but, due to the high computational cost, only one point over eight is considered in the horizontal directions. In the vertical direction all the 22 levels are seeded from 3 600 m to 14 400 m. To identify WCB trajectories, a criterion of ascent of more than 600 hPa in 48 h is applied following Joos and Wernli (2012).

3) Heating and water vapor mixing ratio budgets

The ICE3 microphysics scheme is composed of more than 20 specific processes. Three among them have much more impact than the others on latent heat release in our simulations and are summarized in table 1. They correspond to the vapor condensation/deposition on droplets/pristine ice, snow, and graupel and were already the key processes in MAZ21. Additionally, the radiative heating/cooling rate is also considered as it has an important effect on the heating budget.

3. Differences between model simulations in microphysics and upper-tropospheric dynamics

Differences between REF and T40 simulations in microphysics and upper-level dynamics are described in the present section and interpreted by analyzing a heating budget.

Abbrevation	Description of process
CDEPI	Condensation/Evaporation and Depositional/Sublimation growth of pristine ice ($rv + ri/rc \leftrightarrow ri/rc$)
DEPS	Depositional/Sublimation growth of snow (Deposition, only in MPCs) ($rv + rs \leftrightarrow rs$)
DEPG	Depositional/Sublimation growth of graupel (Deposition, only in MPCs) ($rv + rg \leftrightarrow rg$)
RAD	Radiative heating/cooling rate

Table 1. Abbreviation of the most important diabatic processes involved in the heating budget.

a. Microphysics properties in the simulations

To visualize the conceptual difference between REF and T40, Fig. 2 shows the thermodynamic phase partition (pristine ice mixing ratio over the sum of droplet and pristine ice mixing ratios) between REF and T40 as a function of temperature. The ratio varies linearly with temperature in T40 as expected by construction of that simulation (Fig. 2 right). The behavior is radically different in REF with the presence of both droplets and pristine ice above -10°C but almost only pristine ice at temperature below -10°C. Such a partition is consistent with Boudala et al. (2004) observations of mid- and high-latitude stratiform clouds who noticed a minimum for liquid fraction around -15°C associated to a maximum in solid fraction. However, in our model this partition may be due to the fact that REF creates a positive feedback loop. The first stage of the scheme deals with all the processes except the water vapor deposition on droplets and pristine ice: it includes nucleation, vapor deposition on snow and graupel, hydrometeors collision and conversion, the Wegener-Bergeron-Findeisen (WBF) process (Wegener 1926; Bergeron 1935; Findeisen 1938) and sedimentation. It is during the second stage that vapor deposition on droplets/pristine ice occurs. But since vapor deposition within REF depends on the pristine ice and droplets mixing ratios just before the adjustment, and since the droplets mixing ratio is likely to be low at the end of the first stage potentially because of very efficient snow riming processes, vapor will be preferentially transformed in pristine ice. This prevents droplets to grow and has the resulting effect to widen the gap between pristine ice and droplet mixing ratios. Such an issue has already been noticed by Liu et al. (2011) for the same method used in REF and there is room for improvement of this parameterization.

Figure 3 shows the PDFs of hydrometeor mixing ratios for values larger than 10^{-4} g/kg. The threshold avoids visualizing all the meshes with very low or near-zero values of mixing ratios. T40 has almost twice as many grid boxes with low amounts of cloud droplets and graupel than

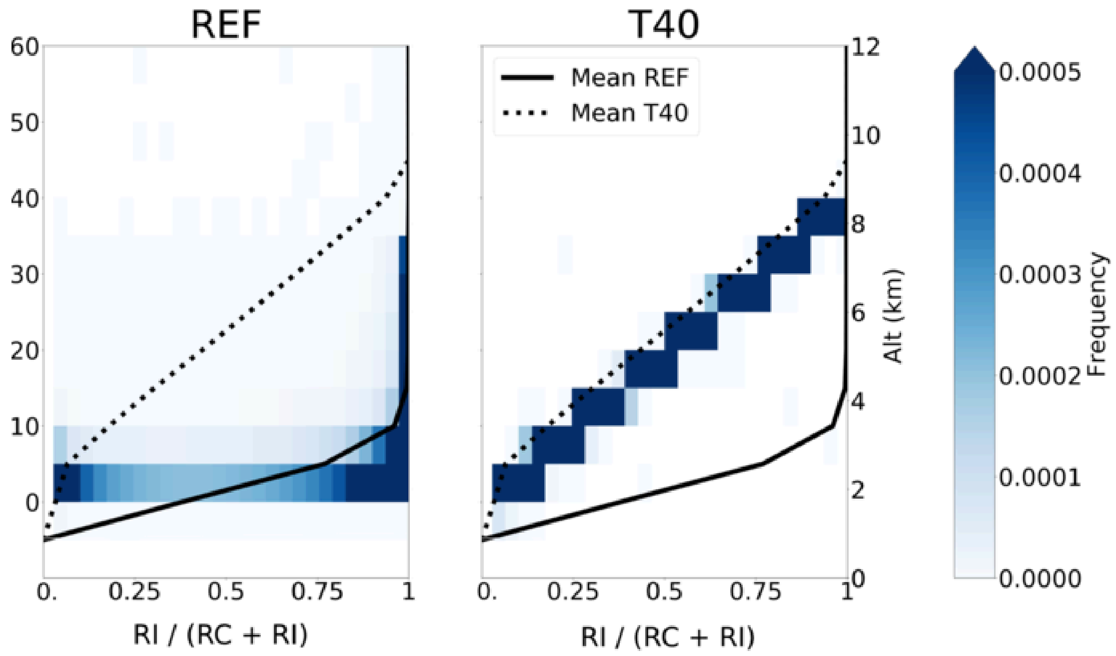

Figure 2. Bivariate PDFs as a function of temperature for partition of pristine ice over sum of cloud droplets and pristine ice over the whole domain using forecast time after 12, 18, 24, 36, 48 hours for the stalactite cyclone simulation initialized at 00 UTC on 1 Oct. Zero value for mixing ratio is not considered in bivariate PDFs calculation. REF is on the left, T40 is on the right, mean values of the ratio are plotted in solid lines for REF and dashed lines for T40.

REF but the amount is the same for high mixing ratios (Fig. 3a). Fig. 3b shows that REF gets three times more meshes with high pristine ice mixing ratios than T40, while T40 has twice more meshes with low pristine ice mixing ratios. The shapes of the PDF distributions for snow (Fig. 3d) are very similar between the two simulations but slightly right shifted toward higher values (a 0.02 g/kg offset) in REF, consequently REF gets higher snow mixing ratios in total. As REF produces more pristine ice more auto-conversion to snow should occur and as T40 produces more droplets more snow conversion into graupel and graupel growth should occur. Finally, the rain PDFs are very similar (Fig. 3e). The PDFs of the total mixing ratios (Fig. 3f) behave similarly as those of snow (Fig. 3d) and the difference between the two PDFs is also largely dependent on snow, then on pristine ice and thirdly on graupel and droplets. To conclude, REF simulates higher mixing ratio values of cold hydrometeors (excepting graupel) but T40 simulates higher mixing ratio of droplets (rain is equal).

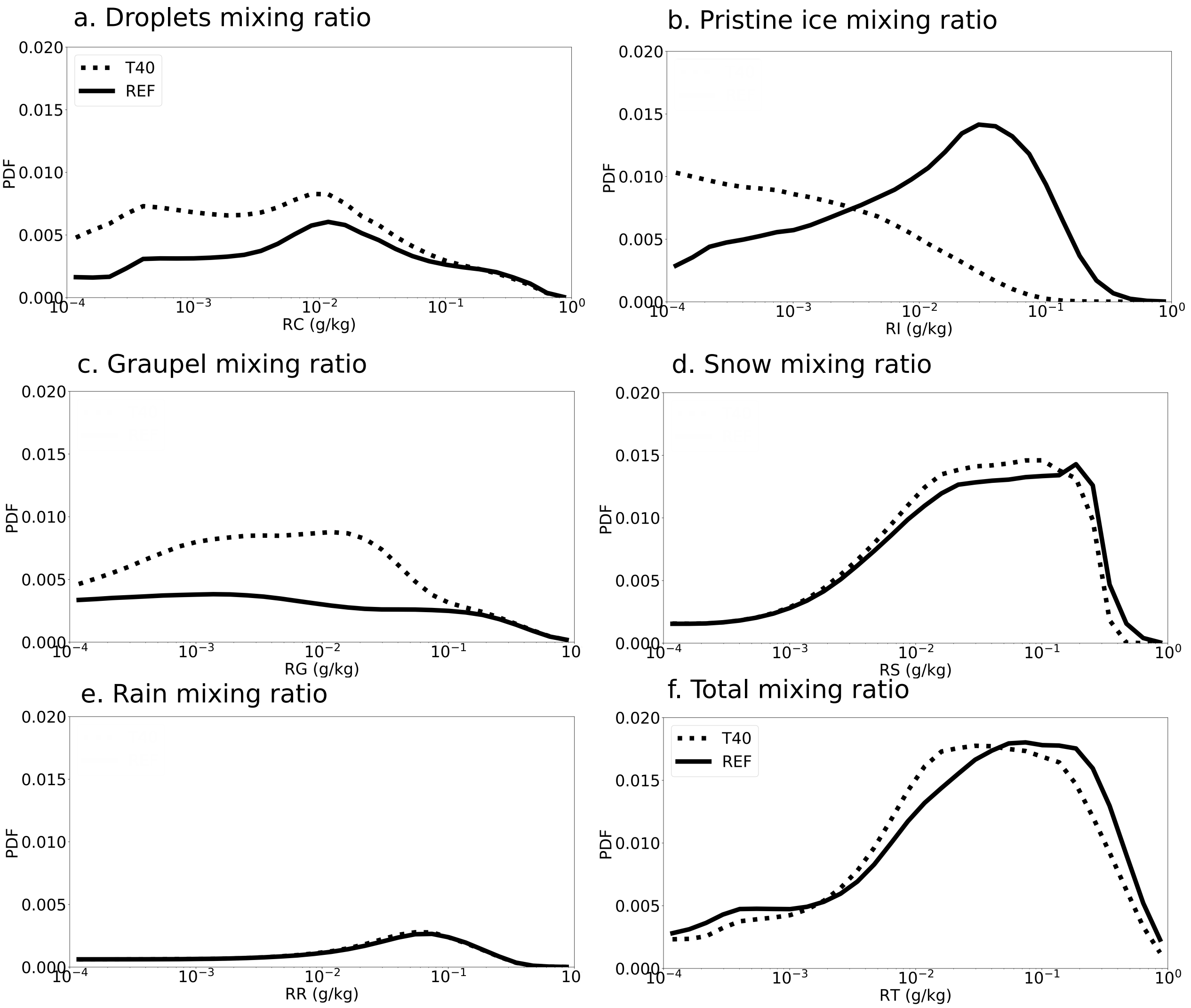

Figure 3. PDFs of mixing ratio of (a) cloud droplets, (b) cloud pristine ice, (c) graupel, (d) snow and (e) total hydrometeor amount (on a log-scale) over the whole domain using forecast time after 12, 18, 24, 36, 48, 60 and 72 hours. REF is plotted in solid lines and T40 in dashed lines.

b. Impact on upper-tropospheric circulation.

In all performed experiments, the difference in MSLP minima between T40 and REF does not exceed 1 hPa. Hence, the surface cyclone is very similar between the two runs. The main purpose of the study is to focus on noticeable differences at upper-levels and their dynamical interpretation. Figures 4a-c represent the upper-level PV differences between REF and T40 at the 315-K isentropic surface for the three types of simulations at 36 h or 48 h valid time depending on the case. The PV anomaly (T40-REF) is positive and has a narrow crescent shape on the western edge of the ridge for all three cases but its extension and intensity vary from case to case. Therefore REF

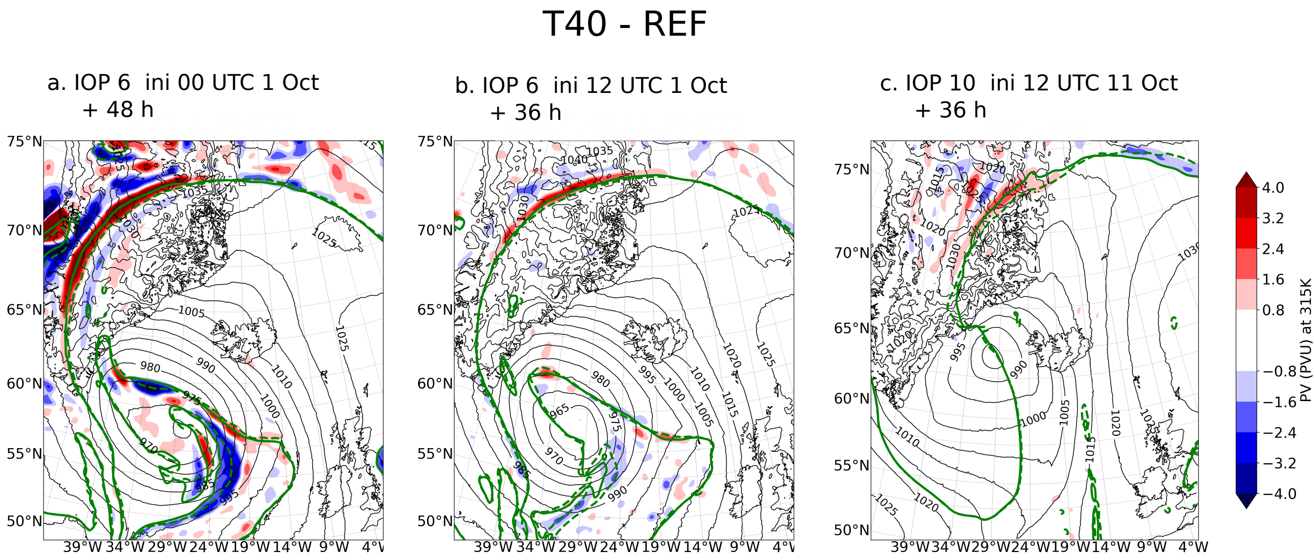

Figure 4. (a)-(c) PV differences between T40 and REF at the 315-K isentropic surface (shading; units: PVU) and SLP at (a-b) 00 UTC 3 Oct and (c) 00 UTC 13 Oct. The initial conditions are (a) 00 UTC 1 Oct, (b) 12 UTC 1 Oct and (c) 12 UTC 11 Oct.

produces a slightly larger ridge than T40 for the three sets of simulations with a tropopause shift varying between 1 ° and 4 ° of longitude locally depending on the case. The case with the largest difference (Fig. 4a) has a PV anomaly of the same order of magnitude as that found in MAZ21 when comparing two distinct microphysical schemes in Meso-NH, and as that shown in Joos and Forbes (2016) when changing other parameters in the microphysical scheme of the IFS model. The partition of thermodynamic phases may hence have a significant impact on the upper-tropospheric circulation.

A simulation called T20 (similar to T40 but with the linear function of temperature evolving between 0 °C and -20 °C) has been made for the stalactite cyclone case initialized at 00 UTC 1 Oct. The PV anomaly between REF and T20 was much weaker than that between REF and T40. This suggests that pristine-ice related processes at upper levels occurring between -20 °C and -40 °C are of importance for the ridge building of the stalactite cyclone, consistent with MAZ21's results (see their Fig. 6). One explanation for the difference between the two initial conditions (Figs. 4a and b) could be that a large part of the latent heat release along the WCB of the stalactite cyclone occurs between 00 UTC and 12 UTC on 1 Oct as shown in MAZ21 (see their Fig. 3). Since the case with initial time at 12 UTC 1 Oct misses that part, it likely explains the smaller impact of mixed-phase parameterization on the ridge building in that case.

c. Interpretation via heating budget

An interpretation for the PV differences between REF and T40 is now provided by comparing their heating budgets for the case presenting the largest anomaly (Fig. 4a). Figures 5a, b and c show the vertically-averaged total heating rate at 18 UTC 2 Oct for REF, T40 and their difference respectively for that case. This time corresponds to a rapid increase in the PV difference between REF and T40 (not shown). The heating rate is on average higher and covers broader regions along the cold and bent-back warm fronts with REF than T40. Figures 5d, e and f show vertical cross sections of the total heating rate averaged between 60°N and 75°N in the region including the western edge of the upper-level ridge and a significant part of the bent-back warm front (region marked with a black box in Figs. 5a-c). The cross sections show that the strong heating area is larger in REF and the peak values of the heating rate are 40% higher in REF than T40.

Lagrangian trajectories, as defined in section 2d, are also considered. Seeding of backward trajectories is made at 00 UTC 3 Oct and trajectories are computed over the whole domain shown in Fig.1a but only trajectories satisfying the WCB criterion are retained. In total REF gets a bit more WCB trajectories (10860) than T40 (9531), which corresponds to 12% more trajectories (black and purple dots in Fig. 5a,b). But if we focus on trajectories reaching the PV anomaly on the western edge of the ridge the difference increases. These trajectories are shown in purple in Figs. 5a,b,d,e and satisfy the following criteria at 00 UTC 3 Oct: they belong (i) to the troposphere (PV less than 2 PVU), (ii) to the crescent-shaped PV anomaly shown in Fig. 4a (PV anomaly beyond 1 PVU) and (iii) to the black box shown in Fig. 5. For this subsample of WCB trajectories, REF gets many more trajectories (560) than T40 (217). To conclude, REF generates more heating than T40 in average, this generates more WCB trajectories near the western edge of the ridge in particular, which means more diabatically produced negative PV in the upper troposphere and a more rapid ridge building in REF than T40.

A more accurate scrutiny of the total heating anomaly shown in Fig. 5f reveals that the general stronger heating in REF is not systematic in all regions. Between 40°W and 35°W, the heating rate anomaly exhibits a vertically-oriented dipole with greater heating below 6 km and smaller heating above 6 km in REF. This heating dipolar anomaly, which will be explained with the detailed heating budget of Fig. 6, reinforces the vertical gradient of the heating, thus the more important

PV destruction in REF compared to T40 and therefore participates in the more rapid ridge building in REF.

Table 1 describes the main physical processes involved in the heating budget of Fig. 6 and their abbreviations. For both simulations the main latent heating processes are (1) the depositional growth of droplets and pristine ice (CDEPI), snow (DEPS) and graupel (DEPG) and (2) radiation (RAD) as shown in Fig. 6a. Radiative cooling appears to be of primary importance in the upper troposphere, consistent with Chagnon et al. (2013) and Schäfer and Voigt (2018). The total heating rate is a bit higher in REF than in T40 below 6 km but the reverse happens above. This reveals that the dipolar heating anomaly shown in Fig. 5f between 40°W and 35°W prevails. The total heating budgets of the two schemes differ by about 15 % near the peak at 3 km height and can sometimes exceed 0.04 K/h. These differences are not so large but the relative contributions of the various processes participating in the budget are very different. The higher total heating rate in REF below 5 km is predominantly due to the greater latent heating associated with all depositional processes and also due to the smaller-amplitude radiative cooling. Above 6 km, the higher-amplitude radiative cooling balances the latent heating differences and makes the total heating in REF smaller than in T40.

The sum of latent heating rates due to all depositional processes is higher with REF than T40 above 2km height (brown contours in Fig. 6a) because REF exhibits much more vapor depositional growth on pristine ice despite having less depositional growth on droplets, graupel and snow (see DEPS, DEPG and CDEPI in Fig. 6a for the heating rates and DEPS, DEPG, CDEPI RC and CDEPI RI in Fig. 6b for the water vapor budget). Above 3 km, the most important processes are deposition on pristine ice with REF (purple contours in Fig. 5d) and deposition on snow for T40 (blue contours in Fig. 5e). Because T40 has to obey the linear relationship between the ratio of pristine ice and droplet mixing ratios and the temperature, it can not create more deposition of pristine ice. Droplets are lost during the transition to snow and graupel but are continuously replenished via saturation adjustment to the detriment of ice formation. This is why CDEPI RI (deposition on ice) is near zero while CDEPI RC (deposition on droplets) is important in T40 (Fig. 6b). In REF, the heating due to deposition on graupel and snow is negative indicating the dominance of snow and graupel sublimation. In REF, deposition on snow is small because REF produces less MPCs, which are the

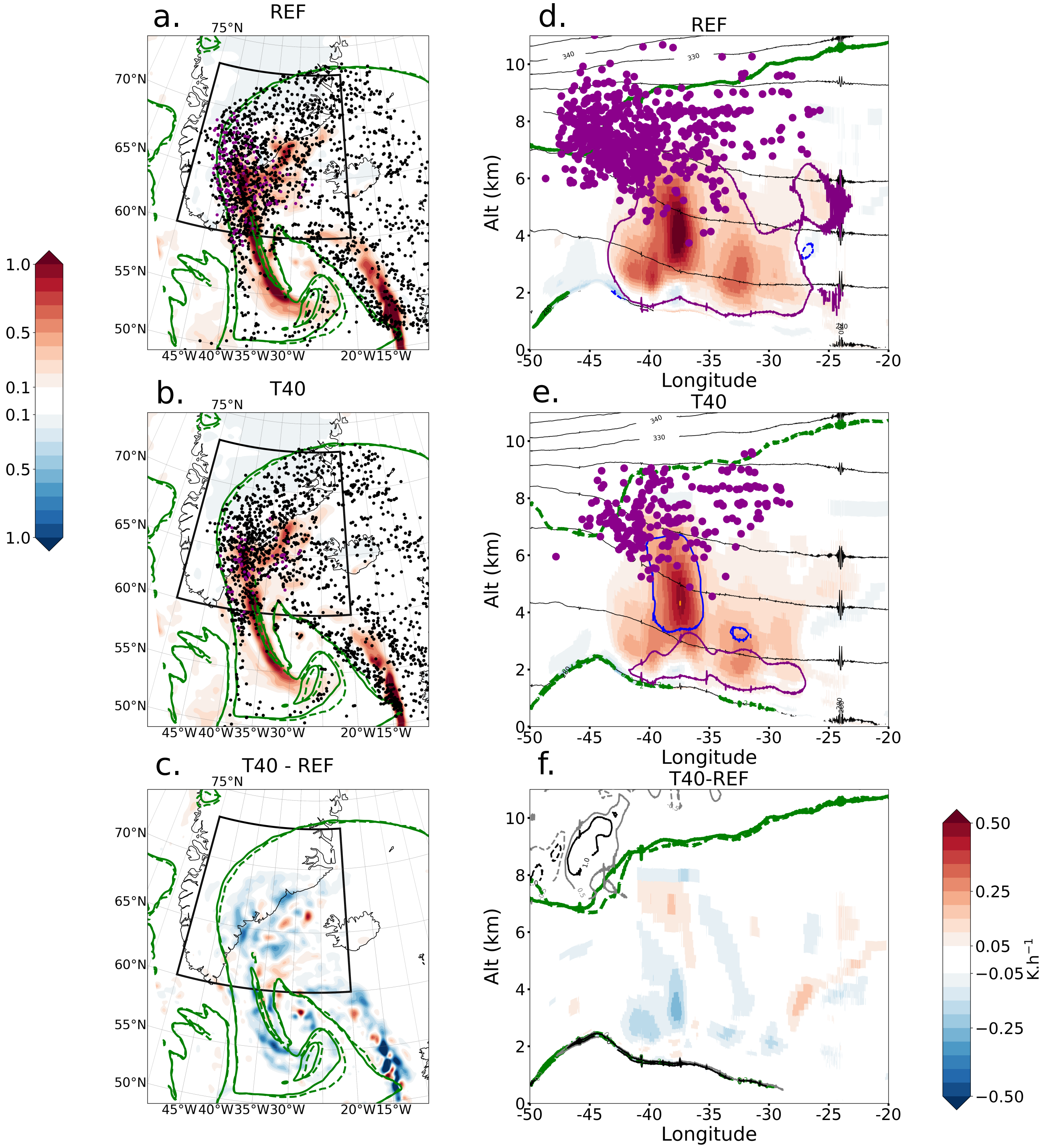

Figure 5. (Left panels) Vertically averaged heating rate between 2 km and 9 km (shadings) and (right panels) meridionally averaged heating rate (shadings) in the large black area shown in upper panels at 18 UTC 2 Oct for (a),(d) REF, (b),(e) T40 and (c),(f) the difference T40-REF. Black dots in (a),(b) correspond to WCB trajectories positions at 18 UTC 2 Oct, while the purple dots correspond to the trajectories ending in the red PV anomaly shown in Fig. 4a. In the upper panels one trajectory in five are represented for visibility sake. Green lines represent the position of the dynamic tropopause (full line in REF and dashed line in T40). The grey and black lines in (f) represent the 1 PVU and 0.5 PVU difference between T40 and REF (solid lines for positive values and dashed for negative ones). The purple and blue contours in (d),(e) represent the CDEPI and DEPS contributions (see Table 1 for their definition) respectively when it is greater than 0.3 $K.h^{-1}$ (solid for positive values and dashed for negative ones).

only cloudy regions where deposition on snow is possible in ICE3, and has thus less opportunities for vapor deposition on snow.

The water vapor budget of Fig. 6b further explains why latent heating due to depositional processes is stronger in REF than in T40. First, there is a slightly larger amount of water vapor deposition in REF in total (black profiles in Fig. 6b). Second, since the deposition on cold hydrometeors is larger in REF than T40 and vice versa for the deposition on warm hydrometeors, latent heat release is larger in REF than T40 for an equivalent amount of transformed water vapor because the specific latent heat of deposition on ice is larger than that of condensation on droplets (about 10% difference at 0° C; Yau and Rogers 1996).

Even though heating rates due to liquid to solid transitions are higher in T40 than REF they are negligible (included in other processes) and do not compensate the more important vapor to solid transitions in REF. Diagnostic of WBF impact is surprisingly very low. This can be explained by the fact that the efficiency of dry growth of graupel and snow riming to collect droplets prevent the WBF process to occur as in our ICE3 version it occurs in the second last step of the scheme. Moreover, as the saturation adjustment over droplets and pristine ice is the very last step of the scheme, it mostly wipes off the possible effect of the WBF process.

Let us now discuss the difference in radiative cooling in Fig. 6a, which has been checked to be due to longwave cooling (not shown). The radiative transfer code we used does not consider snow, graupel and rain. It is only dependent on pristine ice and cloud droplets. The higher radiative cooling in the upper troposphere in REF is consistent with the higher pristine ice mixing ratio and the larger area covered by the upper clouds. In the lower troposphere, as REF gets more cloud droplets and pristine ice (Fig. 6d) and a broader cloud cover (not shown) it may induce a stronger absorption of surface longwave emission and a less strong cooling maybe restrained by the presence of the broader clouds above. The important impact of radiation on the budget confirms a potential high impact of cloud-radiation interaction and parameterization on upper-level dynamics as already anticipated in Joos (2019).

To summarize, the total heating rate is on average higher in REF than T40 when looking at vertically-averaged maps. Vertical profiles of the heating rate show that REF induces a larger heating in the lower half of the troposphere and slightly more cooling in the upper troposphere. The larger heating in the lower troposphere in REF is due to an overall larger amount of water vapor deposition and a preferred transition toward solid phase, which is not compensated by liquid-to-solid transitions in T40. Such a difference explains the higher vertical velocities in REF (Fig. 6c) and the more numerous WCB trajectories in the WCB outflow region. The more important cooling in the upper troposphere in REF is due to the larger amount of pristine ice. Overall, these differences in the vertical profiles of the heating rates will favor more PV destruction in REF than T40 and a more rapid ridge building.

4. Comparison between model simulations and observations

The present section is dedicated to the comparison to observations and pursues two goals: (i) document the locations of the supercooled droplets and the mixed-phase region in extratropical cyclones and how they are represented by Meso-NH and (ii) identify which of the two parameterizations for mixed-phase clouds is the closest to the observations.

a. Thermodynamic phases

Figure 7 presents the thermodynamic phase distribution as retrieved by the RALI platform along the flights F7 and F15 and as simulated by REF and T40 for the different sets of simulations along the flight tracks. To compare with the classification made with the observations (Cazenave et al. 2019), we need to categorize clouds in the model and to define MPCs. Even though there is no unique way to define MPCs (see discussion in Korolev et al. 2017), we adopt a definition close to Korolev et al. (1998) using a threshold in the ratio between Liquid Water Content (LWC) and total water content. Three categories of clouds are defined as follows: liquid phase (LWC > 0 $\mathrm{g.m^{-3}}$ and T > 0 °C), mixed phase (LWC/(LWC+IWC) ¿ 5% and T < 0 °C), ice phase (LWC/(LWC+IWC) ¡ 5%). The choice of the 5% threshold is rather arbitrary and should be taken with caution.

Let us first describe the MPCs detected in the observations. As the lidar is not able to detect multiple layers of supercooled droplets and is subject to attenuation (see section 2c), the black line in Figs. 7a and f, represents the lowest level for mixed-phase layer detection. The melting layer located below the black line is detected by the radar only. Between the black line and the melting layers, we have no information on the presence or absence of mixed-phase layer. Observations out of these blind areas show that MPCs occur in few discrete layers of hundreds meters in agreement with Hogan et al. (2003). Their location occur in four kinds of area:

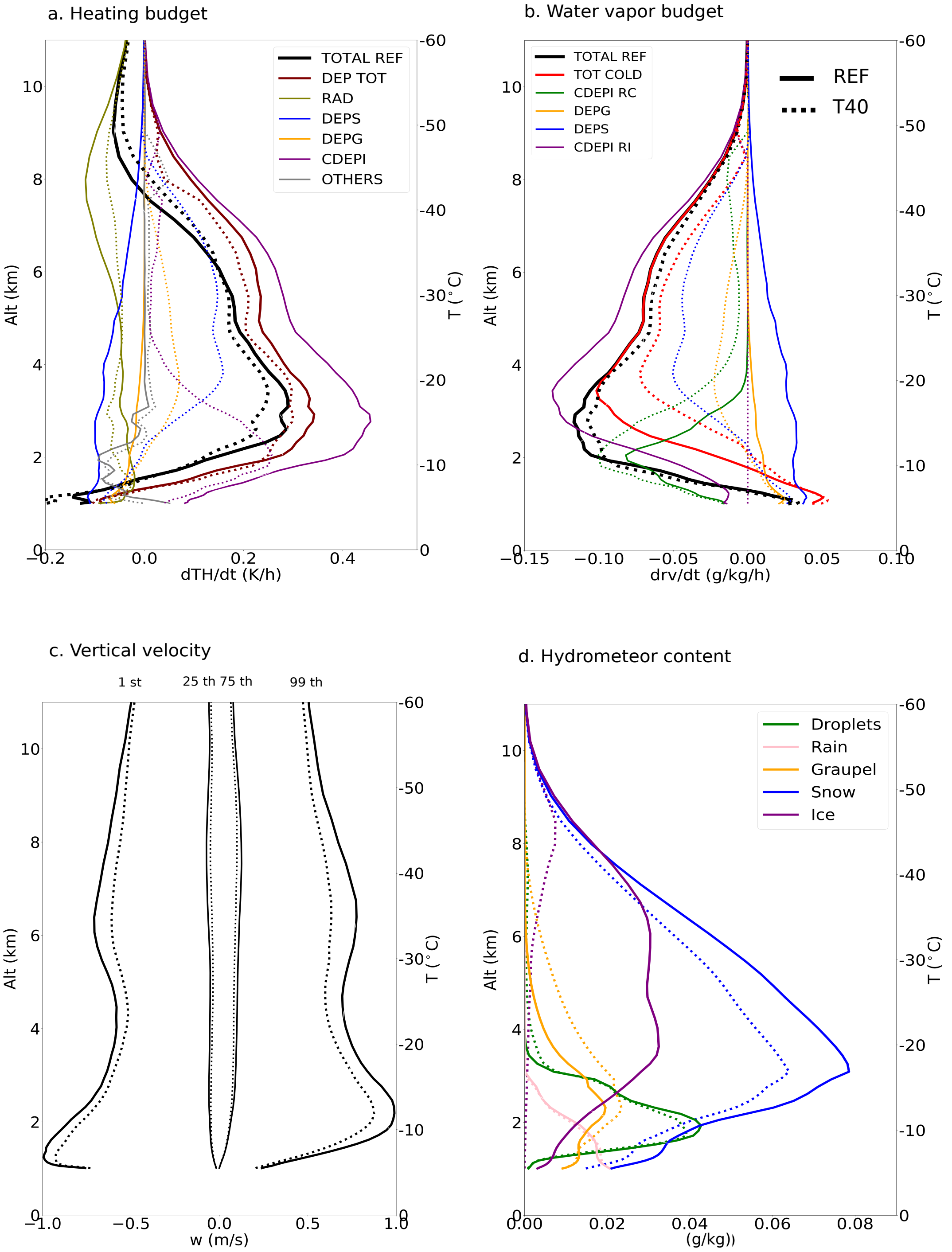

Figure 6. (a) Horizontal average of the heating rate over the box defined in Figs. 5a-c at 18 UTC 2 Oct for total absolute values greater than 0.0 K.h^{-1}. In (b), (c) and (d) statistics are made over the same area and the same time as in (a). Only the main processes are plotted and explained in Table 1, OTHERS corresponds to the sum of all the other processes. (b) Horizontal average of the vapor mixing ratio tendencies. CDEPI RC/DEPG/DEPS/CDEPI RI correspond to deposition of vapor on droplets/graupel/snow/pristine ice respectively. TOT COLD combines all the cold processes. Total is the sum of all the tendencies. (c) 1st, 25th, 75th and 99th percentiles of the vertical velocity distribution. (d) Horizontal average of hydrometeor mixing ratios: RCT, RRT, RGT, RST and RIT correspond to droplets, rain, graupel, snow and ice mixing ratios. Full lines stand for REF and dotted ones for T40.

- at the top of layer of ice crystals (F15 and notably under the dry intrusion between 1630 UTC and 1715 UTC) consistently with most of the observations from literature (Shupe et al. 2008).
- embedded within a layer of ice crystals (F7 at 1315 UTC).
- within a layer of ice crystals with clear air above (F7 at ~ 1405 UTC, ~ 1420 UTC, ~ 1600 UTC and F15 at ~ 1720 UTC).
- at the melting layer.

MPCs could be formed according to distinct processes. Liquid watersaturation conditions at cloud top may be achieved because of radiative cooling or turbulent mixing with clear air according to Korolev and Mazin (2003). Their potential persistence could be due to low ice freezing nuclei (IFN) inhibiting the pristine ice formation and the WBF process from occurring. MPCs embedded within, or above, a layer of ice crystals, are likely to be due to low IFN concentration (Korolev and Mazin 2003) as well. We assume MPCs exist at the melting layer because melting does not happen all at once.

Cloudy areas are very similar between simulations and observations for the Thor ridge and is very close for the stalactite cyclone initialized on 1 Oct 12 UTC. For the stalactite cyclone initialized earlier, that is on 1 Oct 00 UTC, more discrepancies are observed with more dry areas simulated by the model. This is not surprising as the longer the forecasts last, the larger shifts relative to the observations in the dynamical features are expected.

The Meso-NH representation of MPCs is quite distinct from the observations. Even though the comparison can be largely influenced by the 5% threshold applied to detect MPCs in the model as mentioned above, some conclusions can be brought out that do not depend much on the threshold. First the melting layer is a region of MPCs seen in the radar observations and in the model even though it is thicker in the model in general. REF produces quasi no MPCs above the melting layer apart from very rare points (Figs. 7b, d, g). At these locations very few solid hydrometeors are present (not shown) which subsequently could favor liquid production and persistence consistently with REF behavior (see section 2a). In contrast, T40 produces MPC areas above the melting layer in all simulations but not necessarily in the same places as in the observations.

A significant amount of MPCs are located near ~ 8 km in T40 which precisely corresponds to a temperature of ~ -40 °C (e.g., Figs. 7c and e). At such elevated heights the snow and graupel mixing ratios are very small in such a way that the ratio between liquid and total mixing ratios increases. Therefore, such a layer of MPCs near the -40 °C temperature is likely an artefact of the T40 formulation. Nevertheless, two areas of MPCs in T40 are more physically relevant as seen in the stalactite cyclone initialized on 1 Oct 00 UTC and in the Thor ridge:

- The upper discrete layers observed between 1630 UTC and 1720 UTC in the Thor ridge. They appear in both the observations and T40 (Figs. 7f, h). This area corresponds to the dry intrusion (Fig. 1e). The residence time of the F7 flight in the dry intrusion is less than for F15 (Fig. 1c), hence equivalent MPCs are not detected along F7. But preliminary results using NASA's LAADS DAAC data (cloud top thermodynamic phases and cloud top temperature, not shown) showed that MPCs are indeed located above that part of the dry intrusion close to the cold front for both the stalactite cyclone and the Thor ridge.
- An area of MPCs around 1500 UTC and $\sim$ 6-7 km is simulated in T40 (Fig.7c) even though not detected in the observations (Fig.7a). It actually corresponds to an area where the strongest updrafts of the transect are simulated (not shown). Such a strong updraft allows supersaturation over liquid to be reached as documented by Gehring et al. (2020).

To conclude, even though T40 tends to artificially create MPCs in some areas, it also reproduces MPCs in some observed regions and in regions where MPC's are expected, although not observed, whereas REF simply fails to simulate MPCs above the mixing layer. To assess the skills of the simulations more quantitatively with regard to the observations, reflectivity and IWC are hereafter analysed and compared.

b. Reflectivity and IWC

The model-to-radar and radar-to-model complementary approaches are used as in MAZ21. Despite the fact that IWC and reflectivity represent different moments of hydrometeor size distribution (the third and the sixth ones), this allows one to address the weaknesses associated with the assumptions inherent to both approaches. In the following only ranges of simulated reflectivity and IWC values that can be retrieved at each altitude with RALI are used in our comparison.

In MAZ21, only the Mie scattering theory was used to compute the model reflectivity while, in the present study, both Mie and T-matrix scattering theories are employed. Figure 8 shows the reflectivity as measured below the aircraft and as simulated by REF and T40 with Mie and T-matrix. All simulated reflectivities are lower than the observed ones but the underestimation

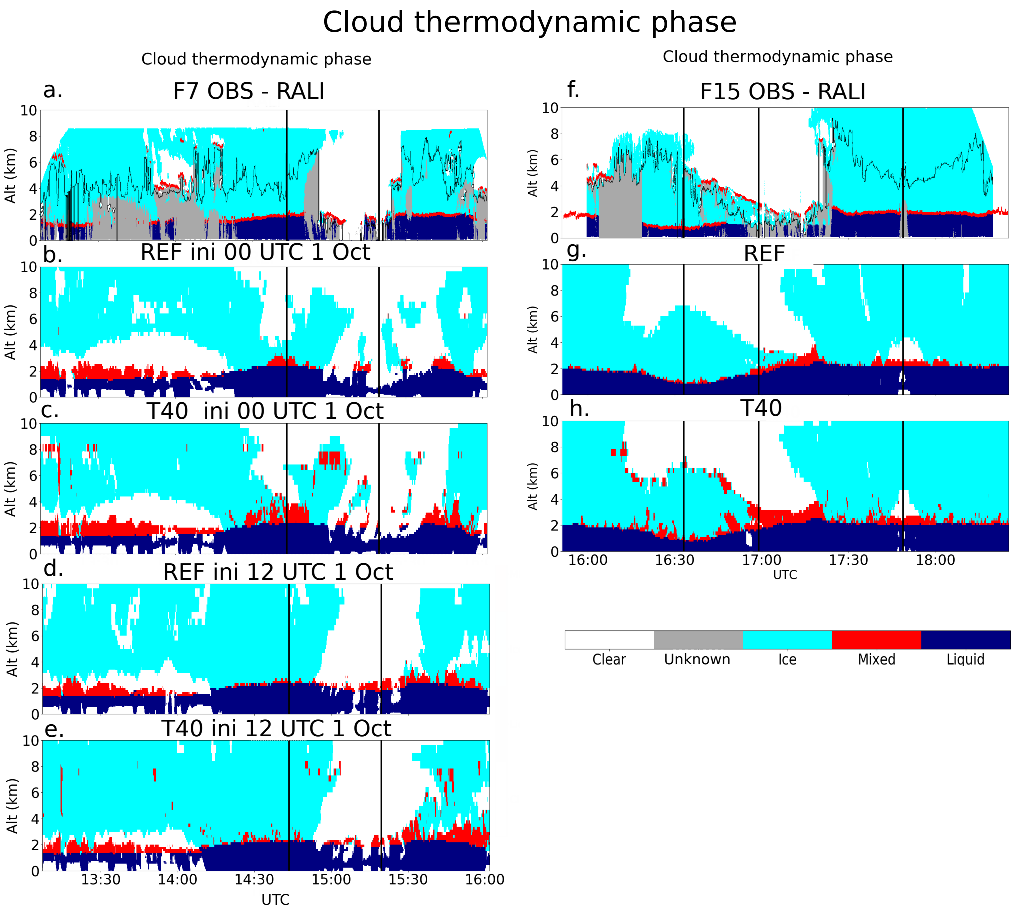

Figure 7. Cloud thermodynamic phase along (a-e): flight F7 (see triangle in Fig. 1d.e), (f-h): flight F15 (see triangle in Fig. 1f) and for: (a.f) RALI observations, (b.g.d) REF simulation and (c.h.e) T40 simulation. (b-c) correspond to stalactite cyclone simulations initialized at 12 UTC on 1 Oct and (d-e) to simulations initialized at 00 UTC on 1 Oct. (g-h) correspond to the Thor ridge simulations. The light dark lines in a and f indicate the bottom attenuation for LIDAR. The vertical bold dark lines stand for the time where the flight changed direction.

is clearly reduced when using T-matrix scattering. For vertically pointing radar, this is because rain, graupel and snow particles are treated as oblate spheroids and have thus a larger maximum diameter, which increases the reflectivity, compared to the Mie theory for which particles are considered spherical. With T-matrix, higher values of reflectivity are thus simulated, bringing the model closer to the observations, which is in agreement with the study of Borderies et al. (2018). Some additional aspects can be further investigated to improve the radar simulator. For instance, the chosen snow axis ratio (0.7) could be lower for higher mixing ratio and could increase the snow contribution to reflectivity and yield to more realistic snow reflectivities.

Figure 9 presents bivariate PDFs of radar reflectivity following the T-matrix theory as a function of altitude for the stalactite cyclone initialized at 00 UTC 1 Oct. Let us first consider the case where all the hydrometeors are considered in the computation of the simulated reflectivity along the flight tracks (Figs. 9a-c). Below the melting layer, the reflectivity values are rather close between REF and T40 and in agreement with the observations. Above the melting layer, in the middle troposphere between 2 km and 6 km, the reflectivities are also close between REF and T40 but they largely underestimate the observed reflectivity, Root-Mean Square Error (RMSE) are as high as 5 dBz. In the upper troposphere, between 6 km and 8 km, T40 still strongly underestimates the observed reflectivity (RMSE is about 8 dBz) but the REF reflectivity is higher than for T40 and is between between T40 and the observations (REF RMSE is about 3 dBz). To isolate the individual hydrometeor contributions to the total reflectivity, Figs.9d-l present successively the reflectivity without the individual contributions of graupel, snow and pristine ice in the model. Graupel contribution is negligible almost everywhere (compare the two upper panels of Fig. 9). In middle troposphere, below 6 km height, reflectivity is mostly due to snow in both REF and T40 while in upper troposphere, above 6 km height, reflectivity is mostly due to snow and pristine ice in T40 and predominantly due to pristine ice in REF.

Figure 10 presents bivariate PDFs of RALI IWC as a function of altitude for the same simulation along the flight tracks, a log scale is used to have a representation similar to the reflectivity which is shown in decibels. The IWC values are quite distinct between REF and T40 with higher values for REF, especially in the upper troposphere where REF is very close to the observations and T40 underestimates the observed IWC (Fig. 10c). As for the reflectivity in Fig. 9, contributions of each hydrometeor to the total IWC are shown in Fig. 10. In middle and upper troposphere, IWC is mostly composed of snow in T40 (compare dotted lines in Figs. 10c, f, i and l) and of both snow and pristine ice in REF (compare thin solid lines in Figs. 10c, f, i and l).

When considering the variations with height of the IWC and reflectivity, T40 presents the closest shape to the observations , the correlation coefficient is about 0.3/00.54 for IWC/reflectivity within ICE3 and about 0.37/0.60 within T40. Indeed, the decrease with height of both IWC and reflectivity values from 3 km and 8 km are more similar to the observations in T40 than REF (Figs. 9c and 10c). The less important decrease with height in REF is attributed to differences in the distribution of hydrometeors as the decrease with height is much smaller without snow contribution than without ice contribution (compare Figs. 9i and 9l and Figs. 10i and 10l). Therefore it suggests that REF may have too much pristine ice relative to snow and the better vertical profile in T40 than REF reveals a better hydrometeor distribution in the former than the latter. This consideration is done realizing that model categorization of pristine ice and snow is somehow arbitrary as they very often have significant overlap where they coexist in terms of particle sizes.

Figure 11 presents the same panels as Figs.9a-c and 10a-c but for the Thor ridge. As for the stalactite cyclone, T40 presents the closest variations with height of the IWC and reflectivity to observations (the correlation coefficient is about 0.32/0.51 for IWC/reflectivity within ICE3 and about 0.4/0.58 within T40) but generally underestimates both quantities between 3 km and 8 km (RMSE is about 2.2 dBz for reflectivity and 0.13 g/m3 for IWC). In contrast, REF exhibits higher quantities than T40 but the decrease with height is further away from the observations than in T40. In the upper troposphere, IWC in REF, and to a lesser extent the reflectivity, are overestimated RMSE for reflectivity is about 2.8 dBz and 0.02 g/m3 for IWC) whereas in the middle troposphere the IWC in REF has realistic mixing ratios but the mean reflectivity is strongly underestimated (RMSE is about 0.8 dBz) (Figs. 11c,f). Since the highest values of snow are found in mid and low troposphere and the highest values of pristine ice in the upper troposphere, it indicates there is maybe too much ice compared to snow in REF as already seen in the stalactite cyclone simulation. Another result based on the sensitivity of the reflectivity to the different hydrometeors supports these findings: between 2 km and 6 km, the reflectivity is largely underestimated but not the IWC. In the range of mixing ratio encountered in middle troposphere, the snow reflectivity is higher than for pristine ice for an equal mass (not shown). So an increase in snow and a decrease in ice would help to make the REF curves closer to the observations.

To conclude, the common results of the Thor Ridge and Stalactite cyclone cases are the following: there is maybe too much pristine ice and not enough snow in REF and not enough cold hydrometeors in general in T40. Two additional sensitivity numerical simulations have been performed to confirm this conclusion for REF (see supplementary material). A first sensitivity test was performed by increasing the ice to snow autoconversion in REF for the stalactite cyclone case. It improved the shapes of the distributions for the IWC and reflectivity (Fig. S2) while it decreased their absolute values because of more sedimentation due to more precipitating hydrometeors. It also impacted notably the ridge building and the PV values along the dynamical tropopause through radiative impact (Fig. S1). As snow is not taken into account in the radiation code, a higher ice to snow autoconversion causes a lower cooling at cloud top and a higher cooling at cloud base due to

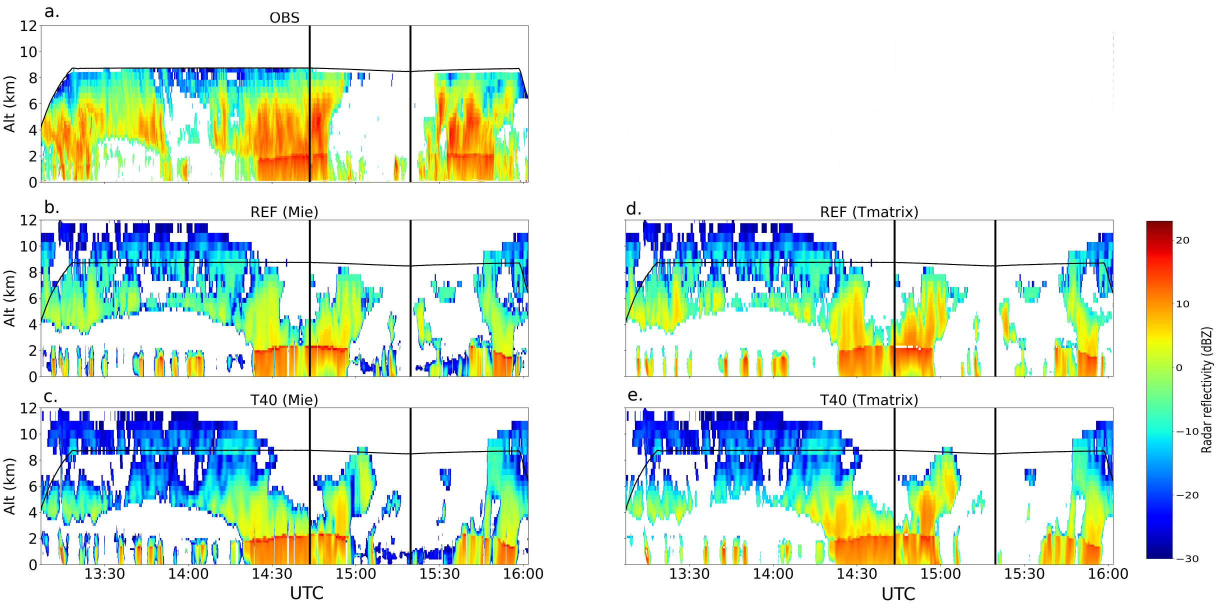

Figure 8. Along F7 (stalactite cyclone), reflectivity for (a) RASTA observations regridded onto the model grid, as calculated with the Mie scattering theory for (b) REF and (c) T40, as calculated with the T-matrix scattering theory for (d) REF and (e) T40. The vertical dark lines stand for the time where the flight changed direction. The simulations are initialized at 00 UTC 1 Oct.

less cloud cover (based only on pristine ice and cloud water). While further investigation should undeniably deepen this aspect, this sensitivity test confirms the potential importance of considering snow in radiation code. Last, but not least, a second sensitivity test was performed by reducing the snow fall speed. It has the effect to increase the atmospheric amount of snow and to improve the distributions with respect to the observations (Fig. S2).

5. Conclusion and discussion

The present study investigates the impact of two mixed-phase cloud parameterizations (REF and T40) developed within the microphysical scheme ICE3 of the Meso-NH model on warm conveyor belts and upper-tropospheric circulation. Three-day hindcast simulations of two extratropical cyclones that developed during IOP 6 and IOP 10 of NAWDEX, and corresponding to the stalactite cyclone and the Thor ridge cases respectively, are performed at a resolution of 2.5-km grid spacing. The differences between the two parameterizations are as follows: in REF deposition of water vapor on droplets and pristine ice is made in proportion to their amount before the saturation adjustment while, in T40, deposition is made in such a way that at the end of all the microphysical steps, the

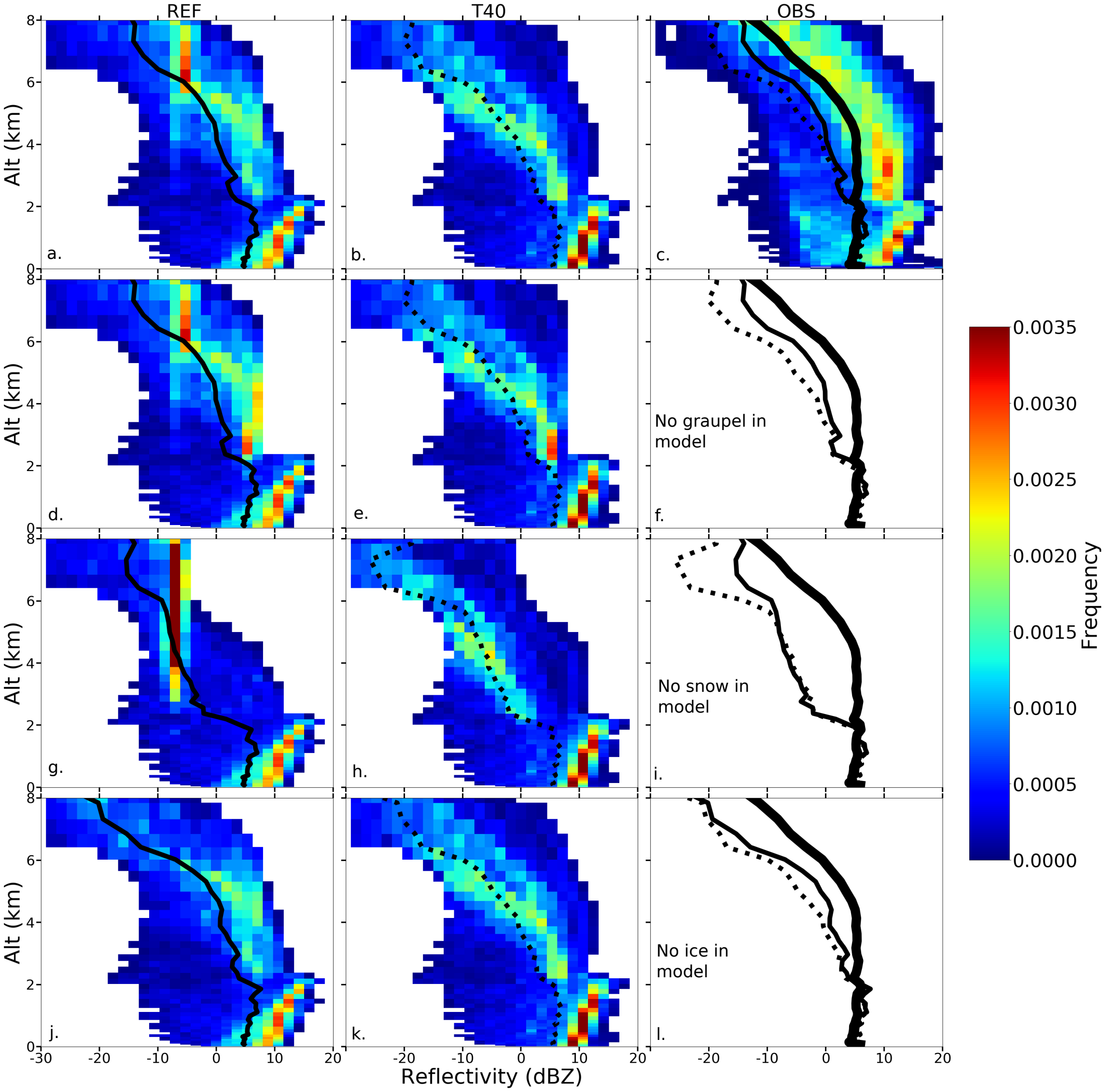

Figure 9. During F7 (stalactite cyclone), bivariate PDFs as a function of altitude of radar reflectivity (a)-(c) total hydrometeors, (d)-(f) without graupel in model, (g)-(i) without snow in model, (j)-(l) without ice in model, (a),(d),(g),(j) REF, T40 and (c),(f),(i),(l) the observations regridded onto the model grid, mean vertical profiles are indicated for REF (solid line), T40 (dashed line), and observations (thick solid line). The measurements and observations are normalized with the total number of points. The simulations are initialized at 00 UTC 1 Oct.

ratio between droplets and pristine ice mixing ratios is a linear function of temperature from 0 to -40 °C.

The first part of the results concerns the impact on the upper-level ridge building in the WCB outflow. REF is found to amplify the ridge more rapidly than T40 even though the amplitude of

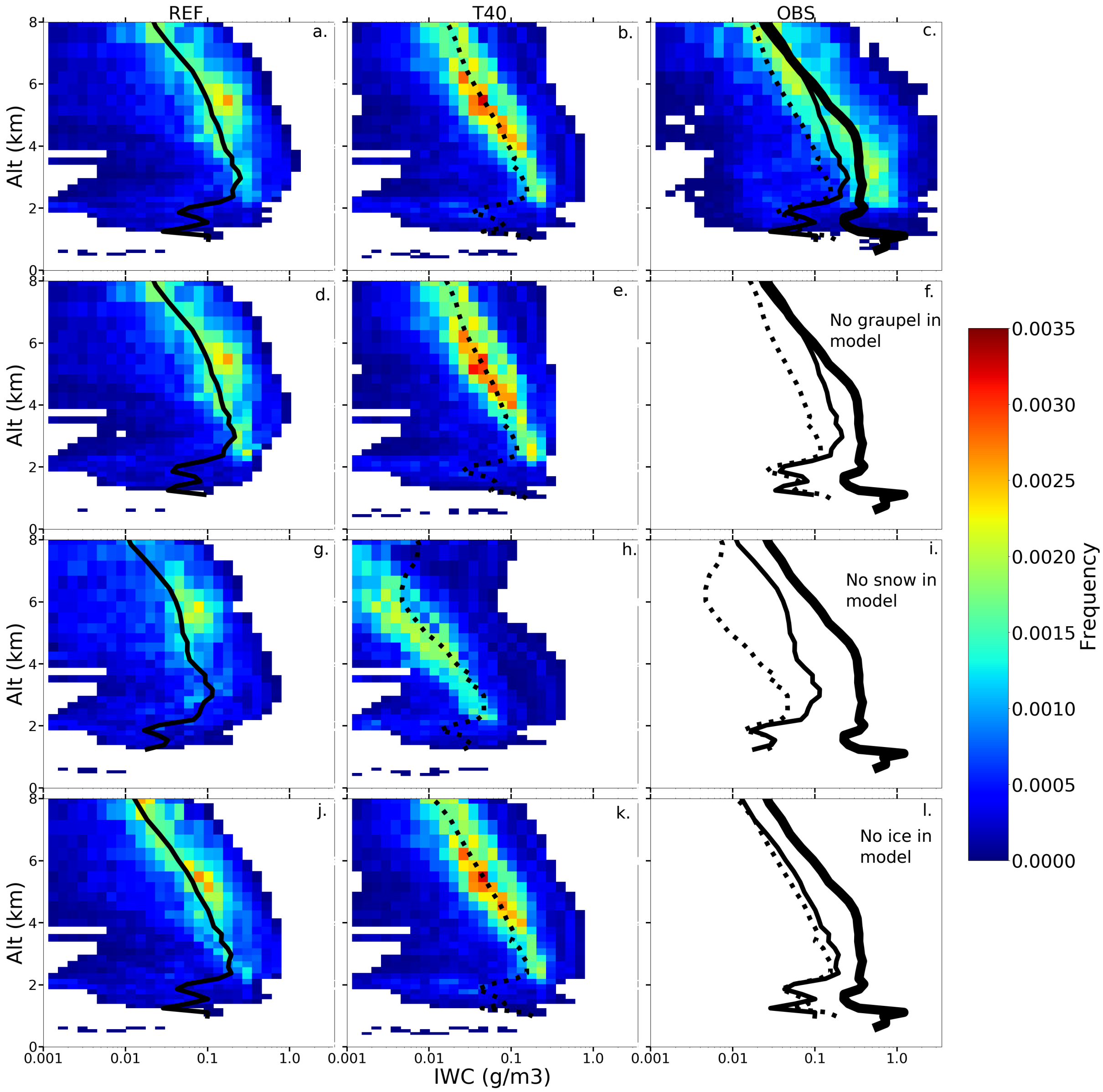

Figure 10. During F7 (stalactite cyclone), bivariate PDFs as a function of altitude of IWC (a)-(c) total hydrometeors, (d)-(f) without graupel in model, (g)-(i) without snow in model, (j)-(l) without ice in model, (a),(d),(g),(j) REF, (b),(e),(h),(k) T40 and (c),(f),(i),(l) the observations regridded onto the model grid, mean vertical profiles are indicated for REF (solid line), T40 (dashed line), and observations (thick solid line). The measurements and observations are normalized with the total number of points.

the PV anomalies between REF and T40 varies from case to case and with the choice of the initial time.

The second part of the results provides an interpretation of the PV differences between REF and T40 based on the simulations of the stalactite cyclone initialized at 00 UTC 1 Oct. It also relies on

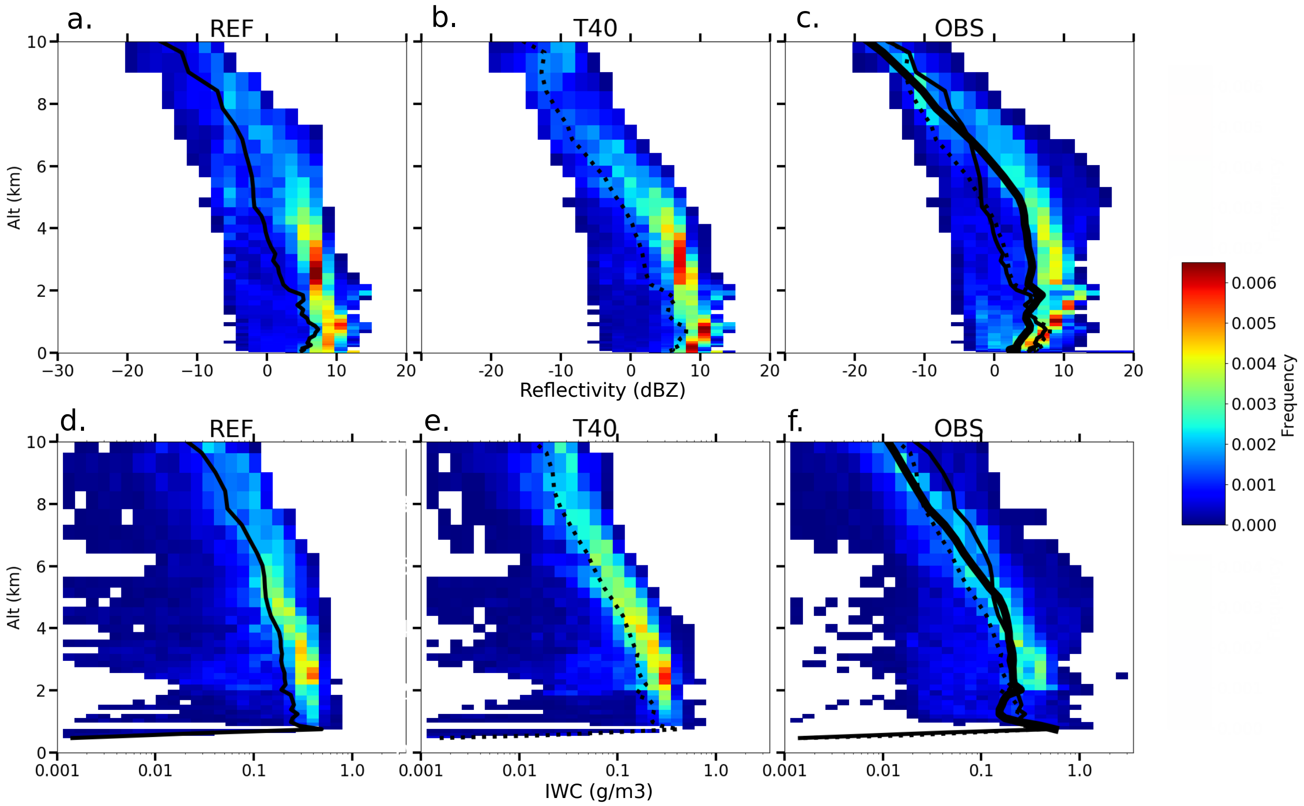

Figure 11. During F15 Thor ridge, Bivariate PDFs as a function of altitude of (a)-(c) radar reflectivity and (d)-(f) Ice Water Content for (a),(d) REF, (b),(e) T40 and (c),(f) the observations regridded onto the model grid, mean vertical profiles are indicated for REF (solid line), T40 (dashed line), and observations (thick solid line). The measurements and observations are normalized with the total number of points.

the computation of Lagrangian trajectories and budgets of hydrometeor mixing ratios and heating rates. The following results were found:

- The vertically-averaged total heating rate is higher in REF than T40 in most regions along the cold and bent-back warm fronts. This explains the higher vertical velocities and the more numerous WCB trajectories found at the leading edge of the ridge building in REF.

- REF exhibits a stronger heating below 6 km height and a more important cooling above 6 km height than T40. The stronger heating in the lower troposphere is due to more important water vapor depositional processes while the larger cooling in the upper troposphere is due to differences in radiative cooling.

- The above differences lead to a stronger vertical gradient of the heating rate in REF that explains the more important PV destruction and more rapid ridge building in REF.

- While differences in horizontal averages of heating rates do not exceed 10 to 20 %, the different processes contributing to the heating rates drastically differ between the two simulations.
- The greater heating rate in REF is due to more water vapor deposition onto ice hydrometeors, which is not compensated by the liquid to solid transitions in T40.
- REF simulates far more pristine ice than T40 but less cloud droplets and graupel. Also, REF simulates more snow that could be due to its higher pristine ice content.
- The larger pristine ice content in REF induces a larger cloud cover and thicker clouds in the upper troposphere that explains the more important radiative cooling at those heights. The difference is well marked because the radiation code does not consider snow. A sensitivity test with an increased autoconversion from ice to snow confirms this result.

The third part of the study is dedicated to the comparison with airborne observations collected during two flights of the SAFIRE Falcon-20 and led to the following results:

- Four main layers of hundred meters of MPCs were detected by the RALI platform at altitude as high as 7 000 m: at the top of pristine ice clouds, embedded within layer of ice crystals, in between a layer of ice crystals below and a layer of clear air above as under the dry intrusion and at the melting layer.
- Both parameterizations reproduce the mixed-phase cloud associated to the melting layer seen in the observations. Well above the melting layer, REF does not form any MPCs whereas T40 does, in particular in regions detected by the radar-lidar platform like below the dry intrusion.
- Comparison of both IWC and reflectivity shows there is maybe too much pristine ice and not enough snow in REF and not enough cold hydrometeors in general in T40. The lower ice to snow ratio in T40 likely explains its better distribution of hydrometeors with respect to height compared to REF.
- Changing the snow fall speed or ice-to-snow conversion are two ways to improve the hydrometeor vertical distribution in REF as confirmed by performing sensitivity numerical experiments (supplementary material).

The present study showed that two different parameterizations of MPC processes have an impact on upper-tropospheric dynamics because they have different latent heat release and radiative cooling within the WCB region. The two parameterizations used in this study have inherent limitations that need to be recalled: in T40 because it forces the MPCs to exist; in REF because it is strongly dependent on ice initiation processes according to Bengtsson et al. (2017); Engdahl et al. (2020) . Indeed if REF first produces a larger ratio of pristine ice compared to cloud droplets, then more vapor deposition will be made on pristine ice limiting the growth of cloud droplets. One way to overcome this limitation is to delay ice formation that should offer larger possibility to droplets to grow and interact with other hydrometeors as done in OCND2 scheme (Bengtsson et al. 2017; Engdahl et al. 2020). The present study shows that to get closer to reality, one would need to better assess distribution of ice, snow, graupel and droplets in mid and upper levels. It could be done by taking advantages of the A-train merged products (CloudSat/CALIPSO/MODIS) which provide thermodynamic phases at cloud top and along vertical transect using DARDAR product (Delanoë and Hogan 2010). In-situ observations (Wurtz et al. 2021; Bernstein et al. 2021) or polarimetric radar would be also very useful to achieve this objective (Gehring et al. 2020). Furthermore, radiative observations may indirectly help to get a better representation of the spatial distribution of hydrometeors. Eventually, an improved representation of hydrometeors in the models is an important issue for climate studies as the distribution of hydrometeors within WCBs has a strong impact on the radiative budget in the mid-latitude as shown in Joos (2019).

Acknowledgements

This work was funded by several projects: EARTHCARE RALI NAWDEX - EPATAN ESA Contract No. 4000119015/NL—CT/gp, CNES AEOLUS/EECLAT, F-NAWDEX of the French national programme INSU/LEFE and ANR DIP-NAWDEX (ANR-17-CE01-0010).

Data Availability Statement

Data available on request from the authors.

References

Alexander, S., G. McFarquhar, R. Marchand, A. Protat, É. Vignon, G. Mace, and A. Klekociuk, 2021: Mixed-phase clouds and precipitation in southern ocean cyclones and cloud systems observed poleward of 64° s by ship-based cloud radar and lidar. *Journal of Geophysical Research: Atmospheres*, **126 (8)**, e2020JD033 626.

Augros, C., V. Caumont, O. Ducrocq, N. Gaussiat, and P. P. Tabary, 2016: Comparisons between S, C, and X band polarimetric radar observations and convective-scale simulations of HyMeX first special observing period. **142**, 347–362, https://doi.org/10.1002/qj.2572, URL http://dx.doi.org/10.1002/qj.2572.

Bengtsson, L., and Coauthors, 2017: The harmonie–arome model configuration in the aladin–hirlam nwp system. *Monthly Weather Review*, **145 (5)**, 1919–1935.

Bergeron, T., 1935: On the physics of clouds and precipitation, proces verbaux de l'association de météorologie, international union of geodesy and geophysics. Paris.

Berman, J. D., and R. D. Torn, 2019: The impact of initial condition and warm conveyor belt forecast uncertainty on variability in the downstream waveguide in an ecwmf case study. *Monthly Weather Review*, **147 (11)**, 4071–4089.

Bernstein, B., and Coauthors, 2021: The in-cloud icing and large-drop experiment science and operations plan. Tech. rep., United States. Department of Transportation. Federal Aviation Administration . . . .

Blanchard, N., F. Pantillon, J.-P. Chaboureau, and J. Delanoë, 2020: Organization of convective ascents in a warm conveyor belt. *Weather and Climate Dynamics*, **1 (2)**, 617–634.

Blanchard, N., F. Pantillon, J.-P. Chaboureau, and J. Delanoë, 2021: Mid-level convection in a warm conveyor belt accelerates the jet stream. *Weather and Climate Dynamics*, **2**, 37–53.

Boettcher, M., and Coauthors, 2021: Lagrangian matches between observations from aircraft, lidar and radar in a warm conveyor belt crossing orography. *Atmospheric Chemistry and Physics*, **21 (7)**, 5477–5498.

Borderies, M., and Coauthors, 2018: Simulation of W-band radar reflectivity for model validation and data assimilation. *Quarterly Journal of the Royal Meteorological Society*, **144 (711)**, 391–403.

Boudala, F. S., G. A. Isaac, S. G. Cober, and Q. Fu, 2004: Liquid fraction in stratiform mixed-phase clouds from in situ observations. *Quarterly Journal of the Royal Meteorological Society: A journal of the atmospheric sciences, applied meteorology and physical oceanography*, **130 (603)**, 2919–2931.

Browning, K. A., 1986: Conceptual models of precipitation systems. *Weather and Forecasting*, **1 (1)**, 23–41.

Caniaux, G., J. Redelsperger, and J. P. Lafore, 1994: A numerical study of the stratiform region of a fast-moving squall line. part I: General description and water and heat budgets. *Journal of the atmospheric sciences*, **51 (14)**, 2046–2074.

Cazenave, Q., M. Ceccaldi, J. Delanoë, J. Pelon, S. Groß, and A. Heymsfield, 2019: Evolution of dardar-cloud ice cloud retrievals: new parameters and impacts on the retrieved microphysical properties. *Atmospheric Measurement Techniques*, **12 (5)**, 2819–2835.

Chagnon, J., S. Gray, and J. Methven, 2013: Diabatic processes modifying potential vorticity in a North Atlantic cyclone. *Quarterly Journal of the Royal Meteorological Society*, **139 (674)**, 1270–1282.

Cober, S. G., G. A. Isaac, and J. W. Strapp, 2001: Characterizations of aircraft icing environments that include supercooled large drops. *Journal of Applied Meteorology*, **40 (11)**, 1984–2002.

Delanoë, J., and R. J. Hogan, 2008: A variational scheme for retrieving ice cloud properties from combined radar, lidar, and infrared radiometer. *Journal of Geophysical Research: Atmospheres*, **113 (D7)**.

Delanoë, J., and R. J. Hogan, 2010: Combined cloudsat-calipso-modis retrievals of the properties of ice clouds. *Journal of Geophysical Research: Atmospheres*, **115 (D4)**.

Delanoë, J., A. Protat, O. Jourdan, J. Pelon, M. Papazzoni, R. Dupuy, J. Gayet, and C. Jouan, 2013a: Retrieval of polar ice cloud properties using rali platform during polarcat campaign. *J. Atmos. Ocean. Tech*, **30**, 57–73.

Delanoë, J., A. Protat, O. Jourdan, J. Pelon, M. Papazzoni, R. Dupuy, J.-F. Gayet, and C. Jouan, 2013b: Comparison of airborne in situ, airborne radar–lidar, and spaceborne radar–lidar retrievals of polar ice cloud properties sampled during the polarcat campaign. *Journal of Atmospheric and Oceanic Technology*, **30 (1)**, 57–73.

DeMott, P. J., and D. C. Rogers, 1990: Freezing nucleation rates of dilute solution droplets measured between- 30 and- 40 c in laboratory simulations of natural clouds. *Journal of Atmospheric Sciences*, **47 (9)**, 1056–1064.

Dirren, S., M. Didone, and H. Davies, 2003: Diagnosis of "forecast-analysis" differences of a weather prediction system. *Geophysical research letters*, **30 (20)**.

Engdahl, B. J. K., G. Thompson, and L. Bengtsson, 2020: Improving the representation of supercooled liquid water in the harmonie-arome weather forecast model. *Tellus A: Dynamic Meteorology and Oceanography*, **72 (1)**, 1–18.

Findeisen, W., 1938: Kolloid-meteorologische vorgänge bei neiderschlags-bildung. *Meteor. Z*, **55**, 121–133.

Flack, D., G. Rivière, I. Musat, R. Roehrig, S. Bony, J. Delanoë, Q. Cazenave, and J. Pelon, 2021: Representation by two climate models of the dynamical and diabatic processes involved in the development of an explosively-deepening cyclone during nawdex. *Weather and Climate Dynamics*, **2**, in press.

Gehring, J., A. Oertel, É. Vignon, N. Jullien, N. Besic, and A. Berne, 2020: Microphysics and dynamics of snowfall associated with a warm conveyor belt over korea. *Atmospheric Chemistry and Physics*, **20 (12)**, 7373–7392.

Gheusi, F., and J. Stein, 2002: Lagrangian description of airflows using Eulerian passive tracers. *Quarterly Journal of the Royal Meteorological Society: A journal of the atmospheric sciences, applied meteorology and physical oceanography*, **128 (579)**, 337–360.

Grams, C. M., and Coauthors, 2011: The key role of diabatic processes in modifying the upper-tropospheric wave guide: a north atlantic case-study. *Quarterly Journal of the Royal Meteorological Society*, **137 (661)**, 2174–2193.

Gray, S. L., C. Dunning, J. Methven, G. Masato, and J. M. Chagnon, 2014: Systematic model forecast error in rossby wave structure. *Geophysical Research Letters*, **41 (8)**, 2979–2987.

Harrold, T., 1973: Mechanisms influencing the distribution of precipitation within baroclinic disturbances. *Quarterly Journal of the Royal Meteorological Society*, **99 (420)**, 232–251.

Hogan, R. J., P. Francis, H. Flentje, A. Illingworth, M. Quante, and J. Pelon, 2003: Characteristics of mixed-phase clouds. i: Lidar, radar and aircraft observations from clare'98. *Quarterly Journal of the Royal Meteorological Society: A journal of the atmospheric sciences, applied meteorology and physical oceanography*, **129 (592)**, 2089–2116.

Hoskins, B. J., M. McIntyre, and A. W. Robertson, 1985: On the use and significance of isentropic potential vorticity maps. *Quarterly Journal of the Royal Meteorological Society*, **111 (470)**, 877–946.

Hu, Y., S. Rodier, K.-m. Xu, W. Sun, J. Huang, B. Lin, P. Zhai, and D. Josset, 2010: Occurrence, liquid water content, and fraction of supercooled water clouds from combined caliop/iir/modis measurements. *Journal of Geophysical Research: Atmospheres*, **115 (D4)**.

Illingworth, A., and Coauthors, 2007: Cloudnet: Continuous evaluation of cloud profiles in seven operational models using ground-based observations. *Bulletin of the American Meteorological Society*, **88 (6)**, 883–898.

Joos, H., 2019: Warm conveyor belts and their role for cloud radiative forcing in the extratropical storm tracks. *Journal of Climate*, **32 (16)**, 5325–5343.

Joos, H., and R. M. Forbes, 2016: Impact of different IFS microphysics on a warm conveyor belt and the downstream flow evolution. *Quarterly Journal of the Royal Meteorological Society*, **142 (700)**, 2727–2739.

Joos, H., and H. Wernli, 2012: Influence of microphysical processes on the potential vorticity development in a warm conveyor belt: A case-study with the limited-area model COSMO. *Quarterly Journal of the Royal Meteorological Society*, **138 (663)**, 407–418.

Korolev, A., J. Strapp, G. Isaac, and A. Nevzorov, 1998: The nevzorov airborne hot-wire lwc–twc probe: Principle of operation and performance characteristics. *Journal of Atmospheric and Oceanic Technology*, **15 (6)**, 1495–1510.

Korolev, A., and Coauthors, 2017: Mixed-phase clouds: Progress and challenges. *Meteorological Monographs*, **58**, 5–1.

Korolev, A. V., and I. P. Mazin, 2003: Supersaturation of water vapor in clouds. *Journal of Atmospheric Sciences*, **60 (24)**, 2957–2974.

Kumar, S., A. Hazra, and B. Goswami, 2014: Role of interaction between dynamics, thermodynamics and cloud microphysics on summer monsoon precipitating clouds over the myanmar coast and the western ghats. *Climate dynamics*, **43 (3-4)**, 911–924.

Lac, C., and Coauthors, 2018: Overview of the Meso-NH model version 5.4 and its applications. *Geoscientific Model Development*, **11**, 1929–1969.

Liu, C., K. Ikeda, G. Thompson, R. Rasmussen, and J. Dudhia, 2011: High-resolution simulations of wintertime precipitation in the colorado headwaters region: Sensitivity to physics parameterizations. *Monthly Weather Review*, **139 (11)**, 3533–3553.

Lord, S. J., H. E. Willoughby, and J. M. Piotrowicz, 1984: Role of a parameterized ice-phase microphysics in an axisymmetric, nonhydrostatic tropical cyclone model. *Journal of Atmospheric Sciences*, **41 (19)**, 2836–2848.

Maddison, J., S. Gray, O. Martinez-Alvarado, and K. Williams, 2019: Upstream cyclone influence on the predictability of block onsets over the Euro-Atlantic region. *Monthly Weather Review*, **147**, 1277–1296.

Madonna, E., H. Wernli, H. Joos, and O. Martius, 2014: Warm conveyor belts in the ERA-Interim dataset (1979–2010). part i: Climatology and potential vorticity evolution. *Journal of climate*, **27 (1)**, 3–26.

Martínez-Alvarado, O., E. Madonna, S. L. Gray, and H. Joos, 2016: A route to systematic error in forecasts of Rossby waves. *Quarterly Journal of the Royal Meteorological Society*, **142 (694)**, 196–210.

Mazoyer, M., and Coauthors, 2021: Microphysics impacts on the warm conveyor belt and ridge building of the nawdex iop6 cyclone. *Monthly Weather Review*, **149 (12)**, 3961–3980.

McFarquhar, G. M., and Coauthors, 2011: Indirect and semi-direct aerosol campaign: The impact of arctic aerosols on clouds. *Bulletin of the American Meteorological Society*, **92 (2)**, 183–201.

Mishchenko, M. I., L. D. Travis, and D. W. Mackowski, 1996: T-matrix computations of light scattering by nonspherical particles: A review. *Journal of Quantitative Spectroscopy and Radiative Transfer*, **55 (5)**, 535–575.

Morrison, H., M. Shupe, and J. Curry, 2003: Modeling clouds observed at sheba using a bulk microphysics parameterization implemented into a single-column model. *Journal of Geophysical Research: Atmospheres*, **108 (D8)**.

Mülmenstädt, J., O. Sourdeval, J. Delanoë, and J. Quaas, 2015: Frequency of occurrence of rain from liquid-, mixed-, and ice-phase clouds derived from a-train satellite retrievals. *Geophysical Research Letters*, **42 (15)**, 6502–6509.

Oertel, A., M. Boettcher, H. Joos, M. Sprenger, H. Konow, M. Hagen, and H. Wernli, 2019: Convective activity in an extratropical cyclone and its warm conveyor belt–a case-study combining observations and a convection-permitting model simulation. *Quarterly Journal of the Royal Meteorological Society*, **145 (721)**, 1406–1426.

Pinty, J., and P. Jabouille, 1998: A mixed-phase cloud parameterization for use in mesoscale non-hydrostatic model: simulations of a squall line and of orographic precipitations. *Conf. on Cloud Physics*, American Meteorological Society Everett, WA, 217–220.

Pomroy, H. R., and A. J. Thorpe, 2000: The evolution and dynamical role of reduced upper-tropospheric potential vorticity in intensive observing period one of FASTEX. *Monthly Weather Review*, **128 (6)**, 1817–1834.

Rasp, S., T. Selz, and G. C. Craig, 2016: Convective and slantwise trajectory ascent in convection-permitting simulations of midlatitude cyclones. *Monthly Weather Review*, **144 (10)**, 3961–3976.

Rivière, G., M. Wimmer, P. Arbogast, J.-M. Piriou, J. Delanoë, C. Labadie, Q. Cazenave, and J. Pelon, 2021: The impact of deep convection representation in a global atmospheric model on the warm conveyor belt and jet stream during nawdex iop6. **2021**, 1–32, https://doi.org/10.5194/wcd-2021-38, URL https://wcd.copernicus.org/preprints/wcd-2021-38/.

Rosenfeld, D., and W. L. Woodley, 2000: Deep convective clouds with sustained supercooled liquid water down to-37.5 c. *Nature*, **405 (6785)**, 440–442.

Sánchez, C., J. Methven, S. Gray, and M. Cullen, 2020: Linking rapid forecast error growth to diabatic processes. *Quarterly Journal of the Royal Meteorological Society*, **146 (732)**, 3548–3569.

Schäfer, S. A., and A. Voigt, 2018: Radiation weakens idealized midlatitude cyclones. *Geophysical Research Letters*, **45 (6)**, 2833–2841.

Schäfler, A., and Coauthors, 2018: The North Atlantic Waveguide and Downstream impact EXperiment. *Bulletin of the American Meteorological Society*, **99 (8)**, 1607–1637.

Seifert, A., and K. Beheng, 2006: A two-moment cloud microphysics parameterization for mixed-phase clouds. part 2: Maritime vs. continental deep convective storms. *Meteorology and Atmospheric Physics*, **92 (1)**, 67–82.

Shupe, M. D., and Coauthors, 2008: A focus on mixed-phase clouds: The status of ground-based observational methods. *Bulletin of the American Meteorological Society*, **89 (10)**, 1549–1562.

Smith, P. J., 2000: The importance of the horizontal distribution of heating during extratropical cyclone development. *Monthly weather review*, **128 (10)**, 3692–3694.

Steinfeld, D., M. Boettcher, R. Forbes, and S. Pfahl, 2020: The sensitivity of atmospheric blocking to changes in upstream latent heating–numerical experiments. *Weather and Climate Dynamics Discussions*, 1–32.

Sun, Z., and K. P. Shine, 1994: Studies of the radiative properties of ice and mixed-phase clouds. *Quarterly Journal of the Royal Meteorological Society*, **120 (515)**, 111–137.

Tao, W.-K., J. Simpson, and M. McCumber, 1989: An ice-water saturation adjustment. *Monthly Weather Review*, **117 (1)**, 231–235.

Tremblay, A., P. A. Vaillancourt, S. G. Cober, A. Glazer, and G. A. Isaac, 2003: Improvements of a mixed-phase cloud scheme using aircraft observations. *Monthly weather review*, **131 (4)**, 672–686.

Vié, B., J.-P. Pinty, S. Berthet, and M. Leriche, 2016: LIMA (v1. 0): A quasi two-moment microphysical scheme driven by a multimodal population of cloud condensation and ice freezing nuclei. *Geoscientific Model Development*, **9 (2)**, 567–586.

Wegener, A., 1926: Thermodynamik der atmosphäre. *Anwendung der Thermodynamik*, Springer, 156–189.

Wurtz, J., D. Bouniol, B. Vié, and C. Lac, 2021: Evaluation of the arome model's ability to represent ice crystal icing using in situ observations from the haic 2015 field campaign. *Quarterly Journal of the Royal Meteorological Society*.

Yau, M. K., and R. R. Rogers, 1996: *A short course in cloud physics*. Elsevier.